Journal of Geophysical Research: Atmospheres

RESEARCH ARTICLE
10.1002/2017JD027852

Investigating the Mechanisms Associated With the Evolutions of Twin Extratropical Cyclones Over the Northwest Pacific Ocean in Mid-January 2011

Shen-Ming Fu[1], **Jian-Hua Sun**[2], **Wan-Li Li**[3], **and Yuan-Chun Zhang**[2]

[1]International Center for Climate and Environment Sciences, Institute of Atmospheric Physics, Chinese Academy of Sciences, Beijing, China, [2]Laboratory of Cloud-Precipitation Physics and Severe Storms, Institute of Atmospheric Physics, Chinese Academy of Sciences, Beijing, China, [3]China Meteorological Administration Training Center, Beijing, China

Key Points:
- A case of twin extratropical cyclones that contains an extreme explosive cyclone shows a significant Fujiwhara effect
- Significant differences in the deepening rates of the twin cyclones are mainly due to the contrast in the middle-level and lower level features
- Factors accounting for the rapid deepening of the explosive extratropical cyclone show significant scale-dependent characteristics

Correspondence to:
S.-M. Fu,
fusm@mail.iap.ac.cn

Citation:
Fu, S.-M., Sun, J.-H., Li, W.-L., & Zhang, Y.-C. (2018). Investigating the mechanisms associated with the evolutions of twin extratropical cyclones over the northwest Pacific Ocean in mid-January 2011. *Journal of Geophysical Research: Atmospheres*, *123*, 4088–4109. https://doi.org/10.1002/2017JD027852

Received 9 OCT 2017
Accepted 27 MAR 2018
Accepted article online 30 MAR 2018
Published online 30 APR 2018

Abstract Twin extratropical cyclones that appeared over the northwest Pacific Ocean in mid-January 2011 experienced significantly different transitions: the northern cyclone dissipated rapidly, whereas the southern cyclone developed into an extreme example of an explosive (i.e., rapidly deepening) extratropical cyclone. This event was reasonably reproduced by the fifth-generation Mesoscale Model, and its associated mechanisms were investigated using piecewise potential vorticity inversion and the Zwack-Okossi vorticity budget. Main results are as follows. (i) The extratropical cyclone-included twin cyclone event showed a Fujiwhara effect, during which the two cyclones orbited cyclonically about a midpoint, approached each other, and finally merged. The twin cyclone interactions enhanced the northern cyclone, but weakened the southern cyclone, by inducing warm advection and cold advection, respectively. (ii) Although upper level tropopause folding contributed the most to deepening of the twin cyclones, significant differences in their deepening rates were due predominantly to the contrast between lower level temperature advection and precipitation-related latent heating. (iii) Stronger upper tropospheric positive absolute-vorticity advection and warm advection associated with an upper level jet, and larger latent heating, made geostrophic vorticity of the southern cyclone increase more rapidly than that of the northern cyclone. (iv) Explosive deepening of the southern cyclone showed insensitive responses to its relative configuration with the upper level jet, whereas its rotation enhancement was faster when the cyclone was embedded within the upper level jet. (v) The upper level forcing had a greater influence on the large-scale flow associated with the twin cyclones, whereas the middle-level and lower level forcings were more dominant close to the cyclone core regions.

1. Introduction

1.1. Motivation

Explosive extratropical cyclones (EECs) (Table 1), which have a geostrophically equivalent deepening rate of 24 hPa/24 hr (i.e., 1 Bergeron) (Sanders & Gyakum, 1980), frequently occur over the northwest Pacific Ocean during the Northern Hemisphere cool season (Allen et al., 2010; Black & Pezza, 2013; Qi, 1993). Twin extratropical cyclones, which are defined as the two extratropical cyclones existing simultaneously within the same region (Yamamoto, 2012; Ziv & Alpert, 1995), sometimes also occur over the northwest Pacific Ocean. Generally, it is uncommon for twin cyclones to contain an EEC (Sinclair, 1997; Ziv & Alpert, 1995).

In mid-January 2011, a case of twin extratropical cyclones appeared over the northwest Pacific Ocean. This event was particularly noteworthy because (i) although near to each other and showing remarkable interactions (i.e., a Fujiwhara effect occurred between the twin cyclones; Fujiwhara, 1923), the twin extratropical cyclones experienced significantly different evolutions and (ii) one of the twin extratropical cyclones developed into a rarely seen extreme EEC (Kuwano-Yoshida & Asuma, 2008), which had a maximum deepening rate of up to ~2.7 Bergeron, a minimum sea level pressure (SLP) of ~933 hPa, and a maximum surface wind of ~33 m/s. This means that it was comparable with the intensity of a typhoon (Ying et al., 2014). The focus of this study is therefore the investigation of interactions between the twin cyclones, the mechanisms dominating their significantly different transitions, and the factors and associated mechanisms for inducing the extreme EEC.

1.2. Background

Twin cyclones are interesting phenomena that were first detected in tropical regions (Brand, 1970; Haurwitz, 1951; Keen, 1982). Different definitions have been used to determine twin tropical cyclones (Chen et al., 2010;

Table 1
Abbreviations Used in This Study

Abbreviation	Original terminology	Abbreviation	Original terminology
EEC	Explosive extratropical cyclone	Z-O vorticity budget	Zwack-Okossi vorticity budget
SLP	Sea level pressure	PV	Potential vorticity
PPVI	Piecewise potential vorticity inversion	UL	Upper layer
IL	Interior layer	ESL	Extended surface layer
TA	Effect of absolute-vorticity advection	TB	Effect of temperature advection
TC	Effect of diabatic processes	TCS	Effect of sensible heat
TCR	Effect of latent heating/cooling	TD	Effect of vertical motions
TE	Effect of friction	TF	Effect of the variation of a geostrophic vorticity
TG	Effect of vertical transport of absolute vorticity	TH	Effect of tilting
TI	Effect of stretching	PVU	Potential vorticity unit

Prieto et al., 2003; Schreck & Molinari, 2009), but by any of these definitions, twin tropical cyclones are an uncommon event (Dong & Neumann, 1983; Schreck & Molinari, 2009). They have the potential to experience the "Fujiwhara effect" (Fujiwhara, 1923), where cyclones in relatively close proximity rotate cyclonically around each other and in some instances amalgamating into a single cyclone (Dong & Neumann, 1983; Hoover, 1961; Prieto et al., 2003). This effect can be a source of errors in the forecast of cyclone track, intensity, and structure (Brand, 1970; Jang & Chun, 2013; Liu & Tan, 2016; Ziv & Alpert, 1995).

Twin extratropical cyclones, though studied less often than twin tropical cyclones, may also experience the Fujiwhara effect (Ziv & Alpert, 1995, 2003). The relative rotation of twin extratropical cyclones associated with the Fujiwhara effect can be estimated by a rotation-separation relationship (i.e., the mutual rotation of twin cyclones is proportional to their combined intensities but inversely proportional to their separation), when their separation is less than 1,400 km (Ziv & Alpert, 1995, 2003). The interactions between twin cyclones become increasingly complex when one of the extratropical cyclones is an EEC. The EEC is an important subcategory of the extratropical cyclone that can develop rapidly (Sanders & Gyakum, 1980). During this rapid development of EECs, heavy precipitation, severe winds, and powerful sea waves are often observed (Hirata et al., 2015). These pose serious threats to fishing and shipping industries. Simulation studies based on various models found that latent heating (Davis et al., 1993; Kuwano-Yoshida & Asuma, 2008) and preexisting upper level disturbances (Fu et al., 2014; Hakim et al., 1996) were crucial for their rapid intensification. As reported by Yoshida and Asuma (2004), some extreme EECs could even reach an intensity above 2.5 Bergeron (~3% of the EECs in their study) and had much greater destructive power. To the best of our knowledge, no previous study has investigated twin extratropical cyclones where one cyclone is an extreme EEC (extreme EECs usually show different evolutionary paths from those of the normal EECs; Kuwano-Yoshida & Asuma, 2008). Therefore, a detailed investigation of the case in this study is helpful to understand this type of event.

1.3. Outline of This Paper

The remainder of this paper is structured as follows. Section 2 describes the model setup, the data set used, and the methods behind the calculations and diagnostics. Section 3 shows the model verification and evolution of the twin cyclones. Mechanisms governing the evolution of the twin cyclones are investigated in section 4. The paper concludes with a discussion in section 5.

2. Model Configuration, Data, and Methodology

2.1. Model Configuration

Because of its proven ability to reproduce EECs effectively (Fu et al., 2014; Martin & Otkin, 2004; Parsons & Smith, 2004; Roebber & Schumann, 2011), the fifth-generation Pennsylvania State University National Center for Atmospheric Research Mesoscale Model (MM5, version 3.7) (Grell et al., 1995) was utilized in this study. MM5 is a limited-area, nonhydrostatic, terrain-following sigma-coordinate model designed to simulate/predict mesoscale and regional-scale atmospheric circulation. Two domains with grid spacings of 36 km and 12 km were employed using one-way nesting (i.e., the outer domain provides boundary conditions for the inner domain, while the inner domain has no feedback on the outer domain). Horizontally,

the outer domain had 226 × 190 grid points, and the inner domain had 451 × 379 points; vertically, both domains had 27 levels. The model was initiated 24 hr before formation of the EEC and integrated for 192 hr to cover the entire lifetime of the cyclone. The simple-ice explicit microphysics scheme (Dudhia, 1989) was used in the outer domain, whereas a mixed-phase one (Reisner et al., 1998) was employed in the inner domain. The Grell cumulus scheme (Grell, 1993) was used for both domains. In this study, all analyses and calculations were based on the inner domain output.

2.2. Data

Six-hourly National Centers for Environmental Prediction (NCEP) final (FNL) analysis data with a resolution of 1° × 1° (https://doi.org/10.5065/D6M043C6) were used for both the initial and lateral boundary conditions of the simulation in this study. The 1° × 1° weekly mean optimum interpolated sea surface temperature data from the Climate Diagnostics Center of the National Oceanic and Atmospheric Administration's Cooperative Institute for Research in Environmental Sciences (NOAA-CIRES CDC) (Reynolds et al., 2002) were used for the sea surface temperature conditions. The 0.1° × 0.1° daily Tropical Rainfall Measuring Mission and other satellite rainfall products (3B42) from the National Aeronautics and Space Administration (NASA) (Huffman, 1997) were used to validate the precipitation simulation. Surface, rawinsonde, ship, and buoy observations from the Japan Meteorological Agency (JMA) were employed to improve the simulation through four-dimensional data assimilation (Grell et al., 1995) and to validate the simulation.

2.3. Methodology

2.3.1. Deepening Rate

This study calculated the deepening rate (Sanders & Gyakum, 1980) as follow:

$$\text{deepening}\quad \text{rate} = \frac{p(t-12)-p(t+12)}{24}\cdot\frac{\sin 60^{\circ}}{\sin\left[\frac{\varphi(t-12)+\varphi(t+12)}{2}\right]}, \tag{1}$$

where t denotes the analysis time (in hours), p represents the cyclone's central SLP (in hPa), and φ stands for the latitude of the center of the cyclone.

2.3.2. Piecewise Potential Vorticity Inversion Method

The piecewise potential vorticity inversion (PPVI) method (Davis & Emanuel, 1991) was used to analyze the deepening of the cyclone. The potential vorticity (PV) used here was that defined by Ertel (1942):

$$\text{PV} = (\boldsymbol{\eta}\cdot\nabla\theta)/\rho,$$

where ρ is air density, $\boldsymbol{\eta}$ is absolute vorticity, and θ is potential temperature. The balance equation from Charney (1955) was used in the PPVI analysis; this could retain quantitative accuracy during the rapid cyclogenesis period (Davis et al., 1996).

By inverting the PV anomaly, the far-field flow associated with that PV anomaly could be obtained and hence its corresponding contribution to the total flow determined. A PV anomaly and its far field are different manifestations of the same phenomenon (Fu et al., 2014; Spengler & Egger, 2012).

In this study, the PV budget equation (Koshyk & McFarlane, 1996) was used to attribute different PV anomalies to their respective main sources. The 75% isoline of relative humidity was used to separate the PV anomalies due to diabatic heating and other effects (Fu et al., 2014). A conventional three-way partitioning method (Davis & Emanuel, 1991; Fu et al., 2014; Wu et al., 2011) was employed. This included (i) an upper layer (UL; 650–50 hPa) that was used to focus on PV anomalies associated with upper tropospheric and/or lower stratospheric air (positive PV anomalies were set to zero whenever the relative humidity >75%), (ii) an interior layer (IL; 950–350 hPa) that was designed to isolate the condensation-induced PV (positive PV anomalies were set to zero whenever the relative humidity <75%), and (iii) an extended surface layer (ESL; including PV anomalies in the layer of 950–850 hPa and the lower boundary θ) that was designed to focus mainly on baroclinic processes (positive PV anomalies were set to zero whenever the relative humidity >75%).

2.3.3. Zwack-Okossi Vorticity Budget Equation

The Zwack-Okossi vorticity budget equation is based on the hydrostatic balance, which explicitly links the near-surface variation with forcing above this level (Azad & Sorteberg, 2014; Lupo et al., 1992; Yoshida &

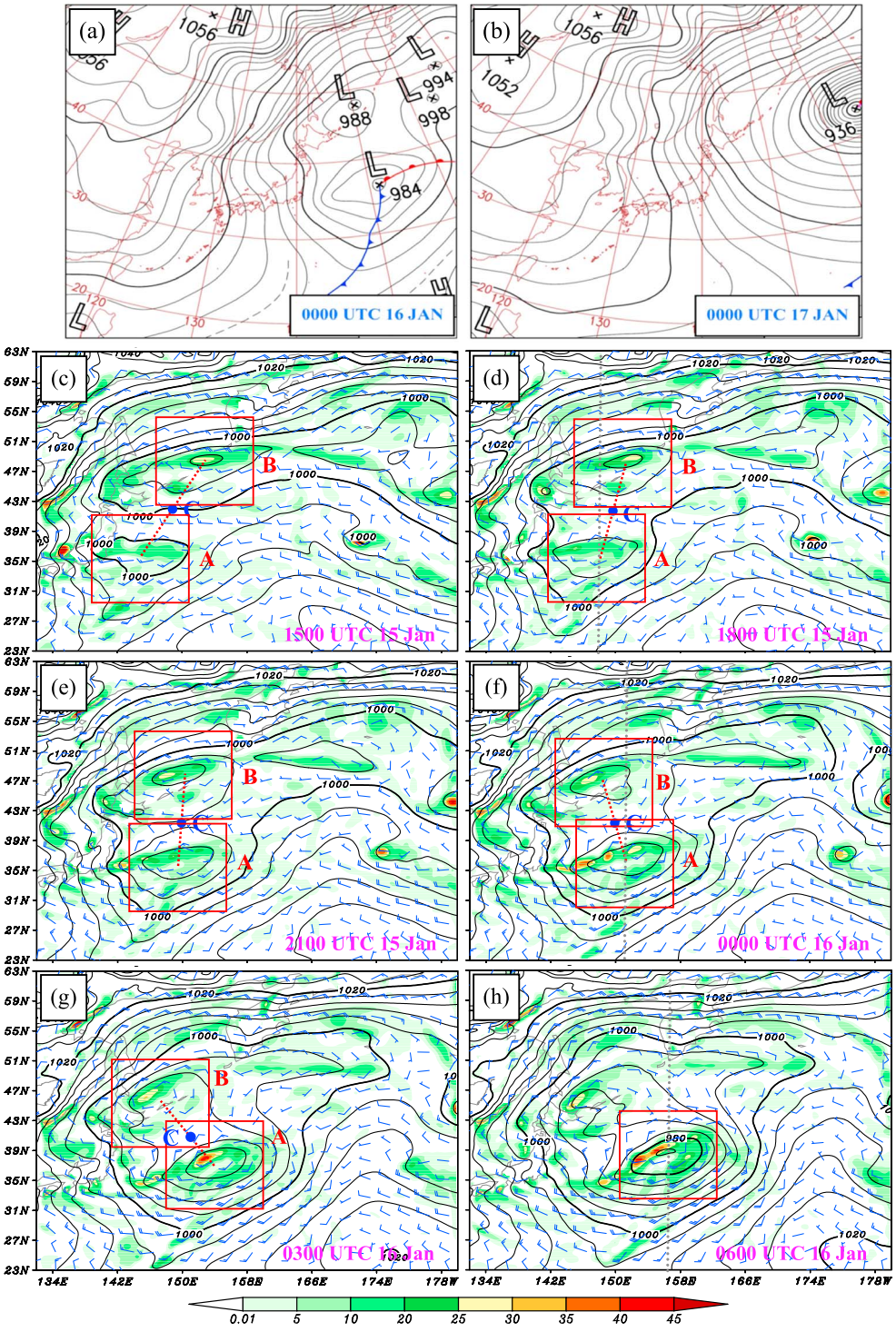

Figure 1. Panels (a–b) show the surface weather charts from the JMA, where the black solid line is the SLP (units: hPa). Panels (c–h) show the simulated SLP (black solid lines, at an interval of 4 hPa), 900-hPa wind (wind bar, with a full bar representing 10 m/s), and 900-hPa geostrophic vorticity (shading; units: 10^{-5}/s), where "A" and "B" show the twin cyclones, "C" represents the midpoint of the twin cyclones, the red box (12° × 12°) marks the key region of twin cyclones, and the grey dashed lines show the location of cross sections of Figures 7a–7c.

Asuma, 2004). In the present study, a complete form of the Zwack-Okossi equation (Lupo et al., 1992) was used to analyze the rotation (geostrophic vorticity) associated with the twin cyclones:

$$\frac{\partial \zeta_{gl}}{\partial t} = Pd\int_{P_t}^{P_l} -\mathbf{V}\cdot\nabla\zeta_a dp \;-Pd\int_{P_t}^{P_l}\left[\frac{R}{f}\int_p^{P_l}\nabla^2\left(-\mathbf{V}\cdot\nabla T+\frac{\dot{Q}}{c_p}+S\omega\right)\frac{dp}{p}\right]dp \;+Pd\int_{P_t}^{P_l}\mathbf{k}\cdot\nabla\times\mathbf{F}dp$$

TA TB TC TD TE

$$-Pd\int_{P_t}^{P_l}\frac{\partial\zeta_{ag}}{\partial t}dp - Pd\int_{P_t}^{P_l}\omega\frac{\partial\zeta_a}{\partial p}dp - Pd\int_{P_t}^{P_l}\left(\frac{\partial\omega}{\partial x}\frac{\partial v}{\partial p}-\frac{\partial\omega}{\partial y}\frac{\partial u}{\partial p}\right)dp + Pd\int_{P_t}^{P_l}\zeta_a\frac{\partial\omega}{\partial p}dp$$

TF TG TH TI

where ζ_{gl} is the geostrophic relative vorticity at a reference level l, p_l is the pressure at that reference level, p_t is the upper level pressure, $Pd = (p_l - p_t)^{-1}$, $\mathbf{V} = u\mathbf{i} + v\mathbf{j}$ is the horizontal wind vector, $\Delta = \frac{\partial}{\partial x}\mathbf{i} + \frac{\partial}{\partial y}\mathbf{j}$, ζ_a is the absolute vorticity, R is the dry-air gas constant, f is the Coriolis parameter, T is the temperature, $\dot{Q}$ is the diabatic heating/cooling rate per unit mass, c_p is the specific heat at constant pressure, $S = -\frac{T}{\theta}\frac{\partial\theta}{\partial p}$, ($\mathbf{i}$, $\mathbf{j}$, $\mathbf{k}$) represent unit vectors pointing to the east, north, and zenith, respectively, $\mathbf{F}$ is the frictional force, ζ_{ag} is the ageostrophic vorticity, and $\omega = dp/dt$. As reported by Lupo et al. (1992), terms TA–TI lead to geostrophic vorticity tendencies at p_l by forcing divergence/convergence at levels above p_l and corresponding spatially varying height decreases/increases at p_l. Terms TA, TG, and TH represent the divergence/convergence produced as the atmosphere readjusts to a geostrophically balanced state in response to local changing vorticity due to horizontal absolute-vorticity advection, vertical absolute-vorticity transport, and tilting effect, respectively. Terms TB, TC (including TCS [effects from sensible heat] and TCR [effects of latent heating/cooling]), and TD represent heating/cooling processes that force horizontally nonuniform upward/downward displacements of the height fields. This results in local divergence/convergence as the atmosphere attempts to reestablish a geostrophically balanced state. Term TF reflects a correction effect accounting for the possibility that the imbalanced atmosphere may attempt to reach a balanced state other than geostrophic. Term TE represents the divergence/convergence due to friction. Term TI denotes the vertically integrated divergence left in place as the atmosphere adjusts to its current state.

3. Model Verification and Evolution of the Twin Cyclones

3.1. Verification of the MM5 Simulation

Comparisons between Figures 1a and 1f show that the simulated twin extratropical cyclones resembled the intensity and location observations well, with maximum intensity and location differences of ~3 hPa and ~100 km, respectively. Evolution of the simulated twin cyclones was consistent with that shown by the NCEP-FNL data: (i) for Cyclone B, both the simulation and FNL show that it began to interact intensely with Cyclone A around 1800 UTC 15 January (Figure 1d) and lost its cyclone structure around 0600 UTC 16 January (Figure 1h); (ii) Cyclone A, which developed into an extreme EEC, formed at 1500 UTC 15 January in the simulation (Figure 2a), ~3 h earlier than that shown by the FNL, while they both dissipated at 1200 UTC 22 January; (iii) the simulation and FNL data both show that Cyclone A moved northeastward before 1200 UTC 19 January and then changed to moving westward (Figure 2a); (iv) the maximum growth rate of Cyclone A occurred during 16–17 January (Figure 2b), with a value of 2.6/2.6/2.7 Bergeron according to the MM5/FNL/observation (Table 2), and then Cyclone A entered a phase of slow variation; and (v) the difference between the minimum SLPs represented by the simulation and FNL was below 3 hPa.

Based on the simulation and NCEP-FNL data, the period of 0000 UTC 16 January to 0000 UTC 17 January was defined as the maximum development stage (Figure 2b). Accumulated precipitation in this stage was verified in Figure 3. It is shown that although the simulated maximum precipitation was weaker than the observation by ~10 mm, the location and distribution of the precipitation observation were well reproduced by the simulation. As mentioned above, the simulation had reproduced key features of the observations reasonably and thus could be used for further studies.

3.2. Representative Factor and Key Region for the EEC

As described in section 2.3.2, PPVI analysis was used to investigate the deepening of Cyclone A. Because SLP was not a direct result from the PPVI analysis, the 900-hPa (above the terrain of the Japanese archipelago) geopotential height was used as an alternative (Azad & Sorteberg, 2014). During the maximum development

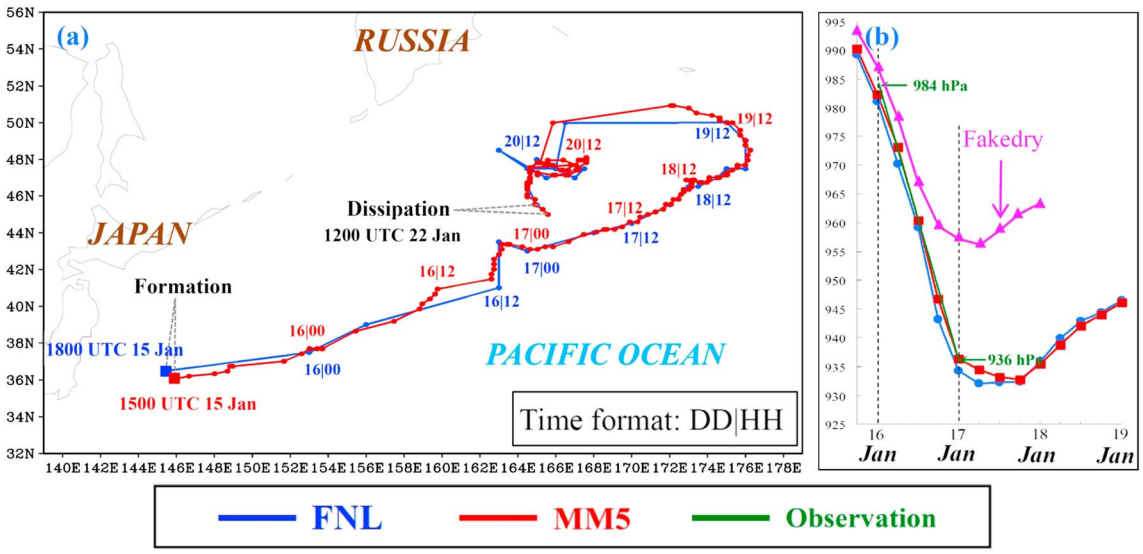

Figure 2. Panel (a) illustrates the MM5 simulated track (red solid, tracked by using the hourly output) and the FNL track (blue solid, tracked by using the six-hourly NCEP FNL data) of Cyclone A. Panel (b) shows the variation of the explosive extratropical cyclone's central SLP (units: hPa), where the red solid line is the result of MM5, the blue solid line is the result of FNL, the green solid line with numbers shows the 24-hourly observation, and the purple solid line is the result of an MM5 fake dry run.

stage, the horizontal averaged 900-hPa geopotential height (in the regions shown in Figure 4a) showed rapid decreasing similar to fast deepening of SLP (Figure 2b). The correlation coefficient between the horizontal averaged 900-hPa geopotential height and the minimum SLP of Cyclone A indicated that these two factors were well correlated with each other (Figure 4b). Therefore, the 900-hPa geopotential height can represent the explosive development of Cyclone A effectively.

To show the overall features of the cyclone, a key region was determined to represent its main body. Thus, a key region averaged factor can be regarded as the cyclone mean feature. As Figure 4b shows, the A2-averaged 900-hPa geopotential height showed the best correlation ($>$0.99) with the minimum SLP of the EEC. As the area grows, the correlation coefficient decreases. In this study, A12 (i.e., a box of size 12 longitudes [~1,000 km] × 12 latitudes [~1,300 km]) was selected as the key region, because (i) this size was close to those of the twin cyclones (Figures 1c–1h) and (ii) A12-averaged 900-hPa geopotential height was highly correlated with the minimum SLP of the EEC, with a correlation coefficient above 0.98 (Figure 4b).

3.3. Overview of the Event

3.3.1. Evolution of The Twin Cyclones

At 1500 UTC 15 January, Cyclone A formed, with a closed isobar of 1,000 hPa appearing in the SLP field and a cyclonic circulation appearing at 900 hPa (Figure 1c). Meanwhile, Cyclone B, which was larger in size, lower in SLP, and stronger in geostrophic vorticity, was located northeast of Cyclone A. At this time, the separation distance between Cyclones A and B was less than 1,600 km (Figure 1c), and a Fujiwhara effect appeared (Fujiwhara, 1923). This is consistent with the result from Ziv and Alpert (1995); that is, when the separation distance is below 2,000 km, an extratropical cyclone pair shows interactions. However, before 1800 UTC 15 January, the cyclone interaction was relatively weak, because the separation distance of the twin cyclones was relatively large (Figure 1c). Strong Fujiwhara effects between the twin cyclones mainly occurred from 1800 UTC 15 January to 0600 UTC 16 January (Figures 1d–1h). This period was defined as the intense interaction stage of this event. At the start of this stage, the centers of Cyclones A and B were ~1,350 km apart (Figure 1d), below the upper limit threshold (i.e., 1,400 km) for the rotation-separation relationship of twin cyclones (section 1.2; Ziv & Alpert, 1995). Then, Cyclones A and B orbited cyclonically about a midpoint and drew closer to each other with time

Table 2
Deepening Rates of Cyclone A During 0000 UTC 16 January to 0000 UTC 17 January and 0000 UTC 17 January to 0000 UTC 18 January 2011 (Units: Bergeron), Based on the NCEP-FNL data, MM5 Simulation, Observation From the JMA, and the Fake Dry Run

	FNL	MM5	Observation	Fake dry run
16–17 January	2.6	2.6	2.7	1.6
17–18 January	−0.1	0.1	0.2	0.2

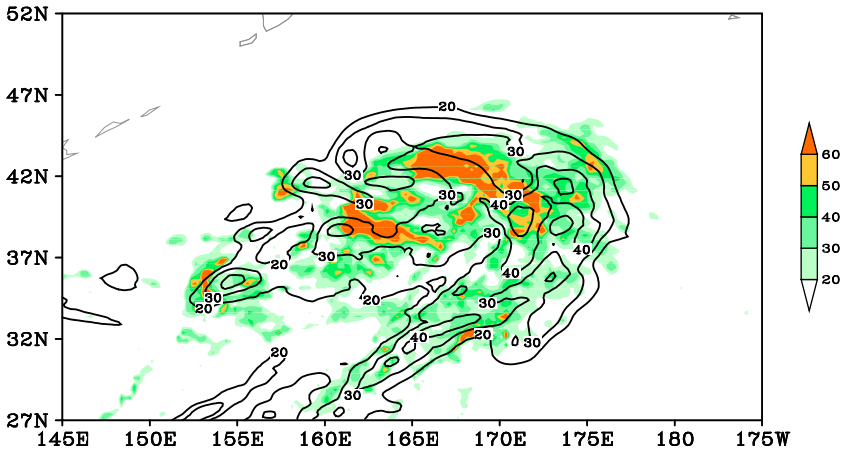

Figure 3. The 24-hr accumulated precipitation associated with Cyclone A, during 16–17 January 2011, where the shading is the Tropical Rainfall Measuring Mission 3B42 daily precipitation estimate (units: mm) and the black solid line is the MM5 simulated precipitation (units: mm).

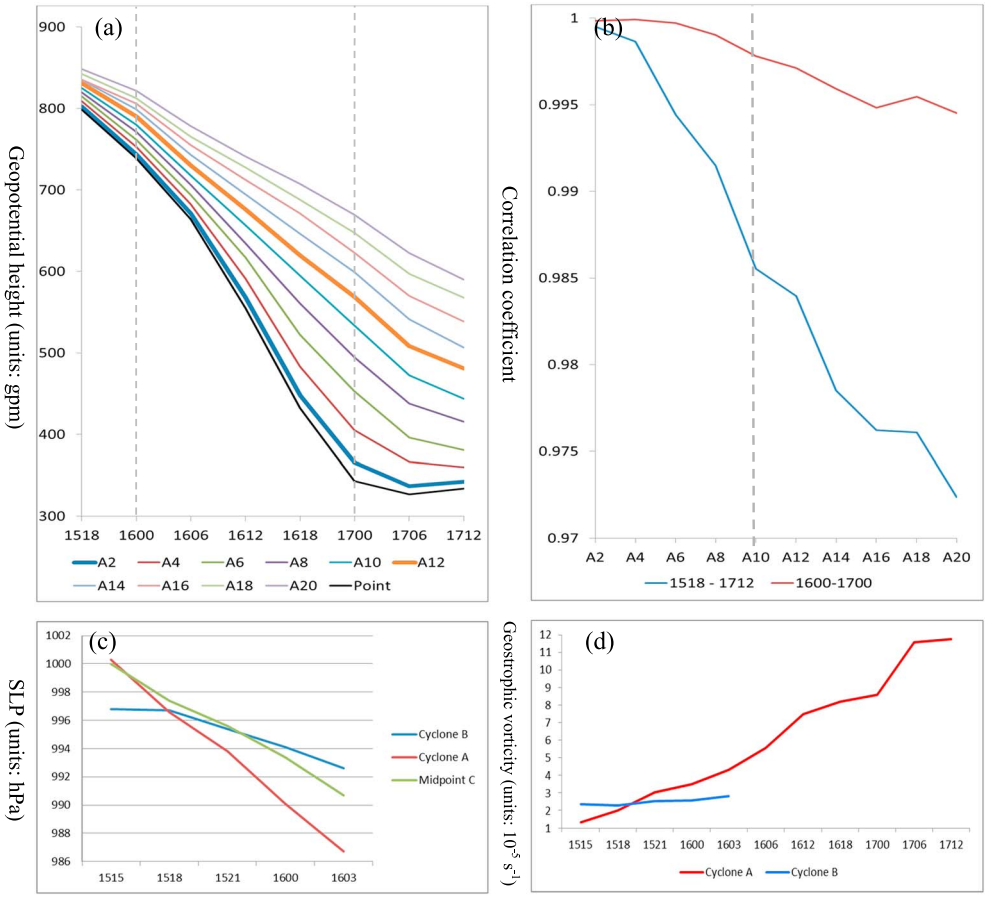

Figure 4. Panel (a) shows the simulated area-averaged 900-hPa geopotential height (units: gpm), where A2 means a 2° (longitude) × 2° (latitude) box centered on the explosive cyclone's center (An has the same meaning, where n = 4…20), and "Point" means the location of the minimum 900-hPa geopotential height. Panel (b) shows the correlation coefficient between the simulated area-averaged 900-hPa geopotential height in panel (a) and the simulated minimum SLP of the explosive cyclone, where the time format is DDHH. Panel (c) shows the simulated SLP at the midpoint C and the simulated key region-averaged SLP of the twin cyclones. Panel (d) illustrates the simulated key region-averaged 900-hPa geostrophic vorticity (units: 10^{-5}/s).

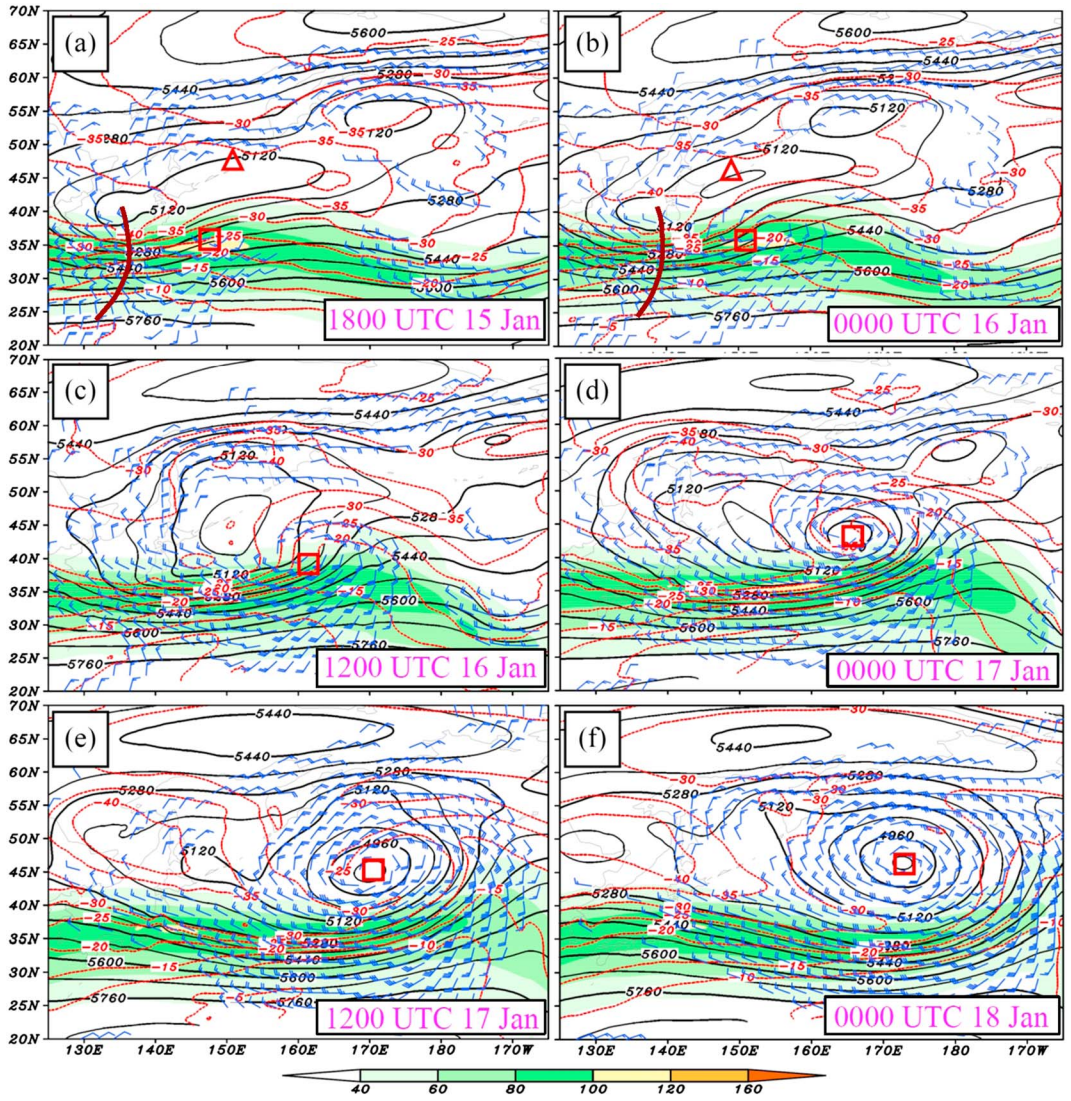

Figure 5. The 200-hPa upper level jet (shading; units: m/s), the 500-hPa geopotential height (black solid line; units: gpm), and temperature (red dashed line; units: °C), as well as the 900-hPa wind above 12 m/s (wind bar; units: m/s), where the red triangle and rectangle mark the centers of the twin cyclones and the thick brown line is the trough line.

(Figures 1c–1g), with a relative angular/radial velocity of ~5°hr · ~24 km · hr. This approximately satisfied the rotation-separation relationship. The patch vortex model (Ziv & Alpert, 1995) is an effective method for estimating the rotation associated with a cyclone. After calculating the area integral of the relative vorticity within a cyclone, the tangential velocity at a distance from the cyclone center can be determined through Green's theorem. This tangential velocity can be used as an estimation of the rotation induced by the cyclone. According to the patch vortex model, in this event, ~75% of the relative rotation of the twin cyclones was due to their interactions. From 0300 UTC 16 January on, Cyclone B began to merge into Cyclone A (Figure 1g). It lost its cyclone structure in terms of SLP at the end of the intense interaction stage (Figure 1h) and had completely merged into Cyclone A by 1800 UTC 16 January.

Cyclone A deepened rapidly at a rate that was approximately 3 times that of Cyclone B (Figure 4c). The 900-hPa geostrophic vorticity of Cyclone A also intensified rapidly (Figure 4d). The correlation between the key region A (red boxes in Figures 1c–1h) averaged SLP and the key region A mean 900-hPa geostrophic vorticity was −0.98/−0.96 during the intense interaction stage/maximum development stage. Thus, the 900-hPa geostrophic vorticity (i.e., the rotation) showed consistent evolution with the rapid deepening of the EEC.

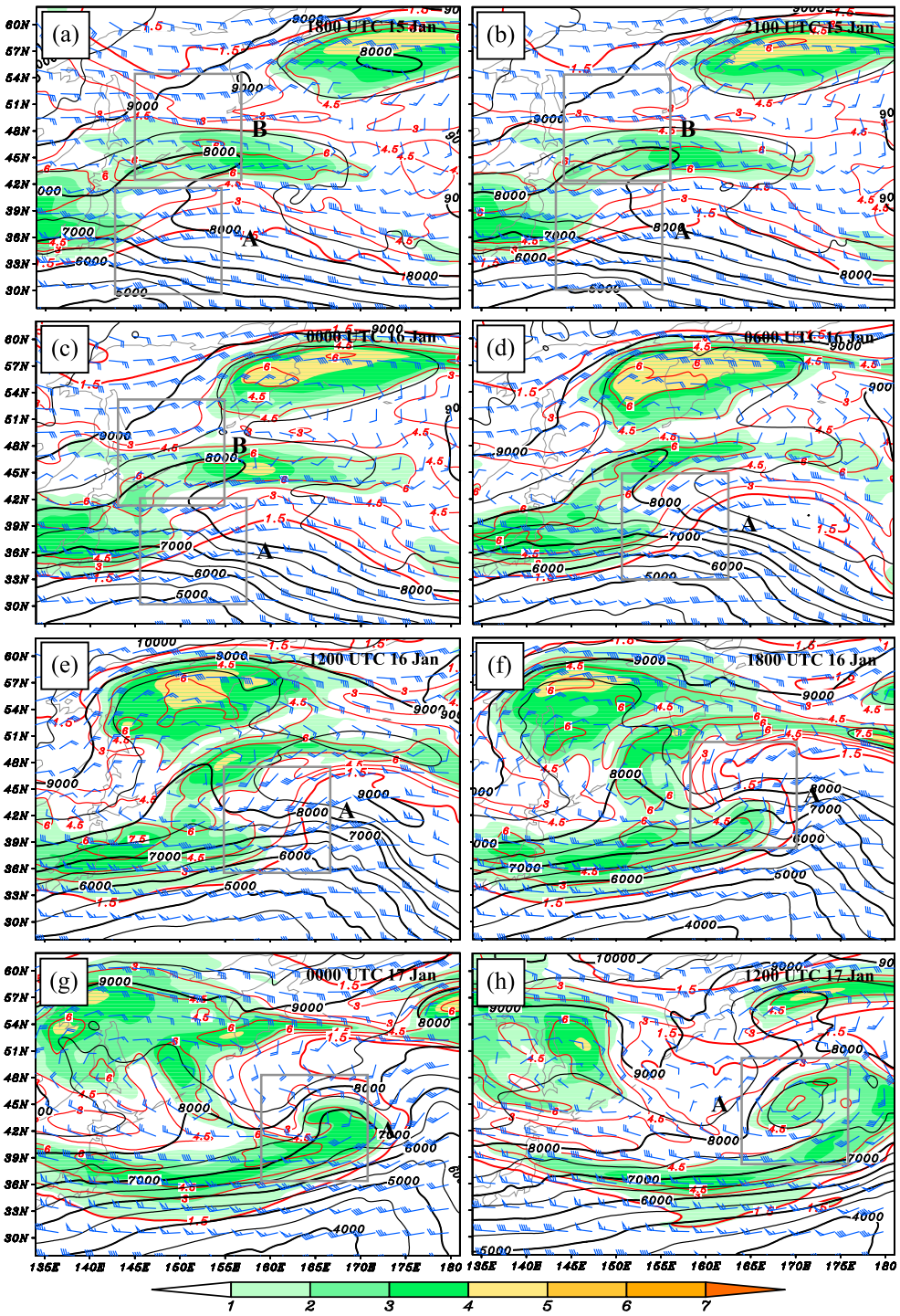

Figure 6. Height (black solid line; units: gpm), PV (red solid line, with an interval of 1.5 PVU), PV anomalies relative to the temporal mean of whole simulation period (shading; units: PVU), and wind field (a full bar is 10 m/s) at the 315-K isentropic surface, where grey boxes mark key regions of the twin cyclone.

In contrast, for Cyclone B, although its SLP lowered significantly, its 900-hPa geostrophic vorticity changed slightly (Figure 4d). Therefore, the evolution of Cyclone B's rotation was not consistent with its deepening.

Overall, before 2100 UTC 15 January, Cyclone B had a stronger geostrophic vorticity and a lower SLP (Figures 1c–1e) than those of Cyclone A, implying that Cyclone B was stronger. However, Cyclone A

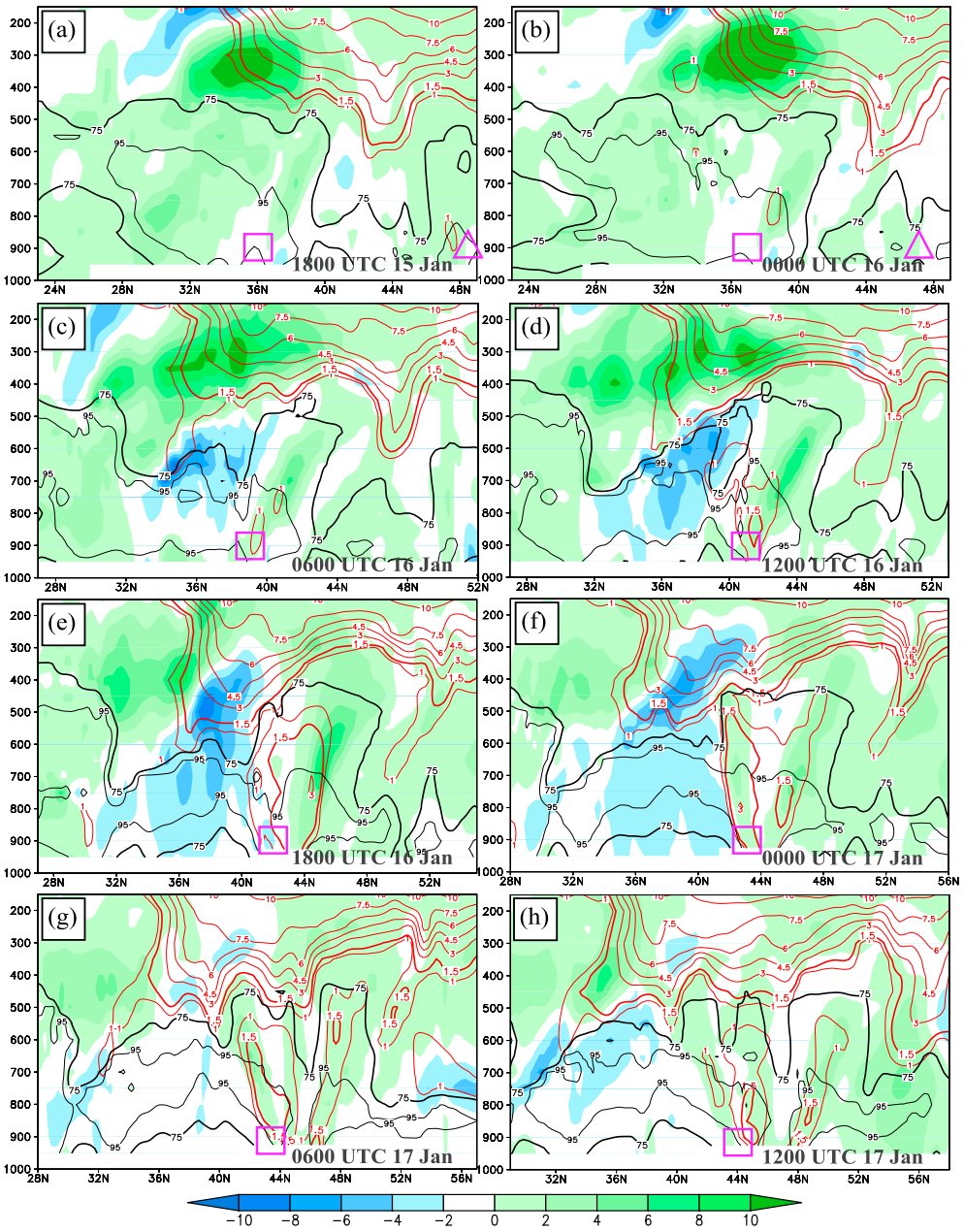

Figure 7. Cross sections along the central longitudes of the explosive cyclone, where the shading is temperature advection (units: 10^{-4} K/s), red solid line is PV (units: PVU), and black solid line is relative humidity (units: %). The purple rectangle and triangle mark the central latitudes of Cyclones A and B, respectively.

intensified much more rapidly than Cyclone B (Figures 4c–4d). As a result, after 2100 UTC 15 January, Cyclone A was the stronger of the two. This reversal of intensity in the twin cyclones caused Cyclone B to lose its advantage and merge into the rapid developing Cyclone A.

3.3.2. Synoptic Background of The Twin Cyclones

In the upper troposphere, a zonally stretched 200-hPa upper level jet maintained quasi-stationary behavior within 25–40°N (Figures 5a and 5b). Tropopause folding (1.5 PVU [= 10^{-6} $m^2 \cdot K \cdot kg \cdot s$] was used as the tropopause) occurred north of the upper level jet (Figures 6a–6c), between the twin cyclones (Figures 7a and 7b). This resulted in a positive PV anomaly (>2 PVU) between these two cyclones (Figures 6a– 6c). In addition, a positive PV anomaly (>3 PVU) appeared west of the key region A, corresponding to the tropopause folding

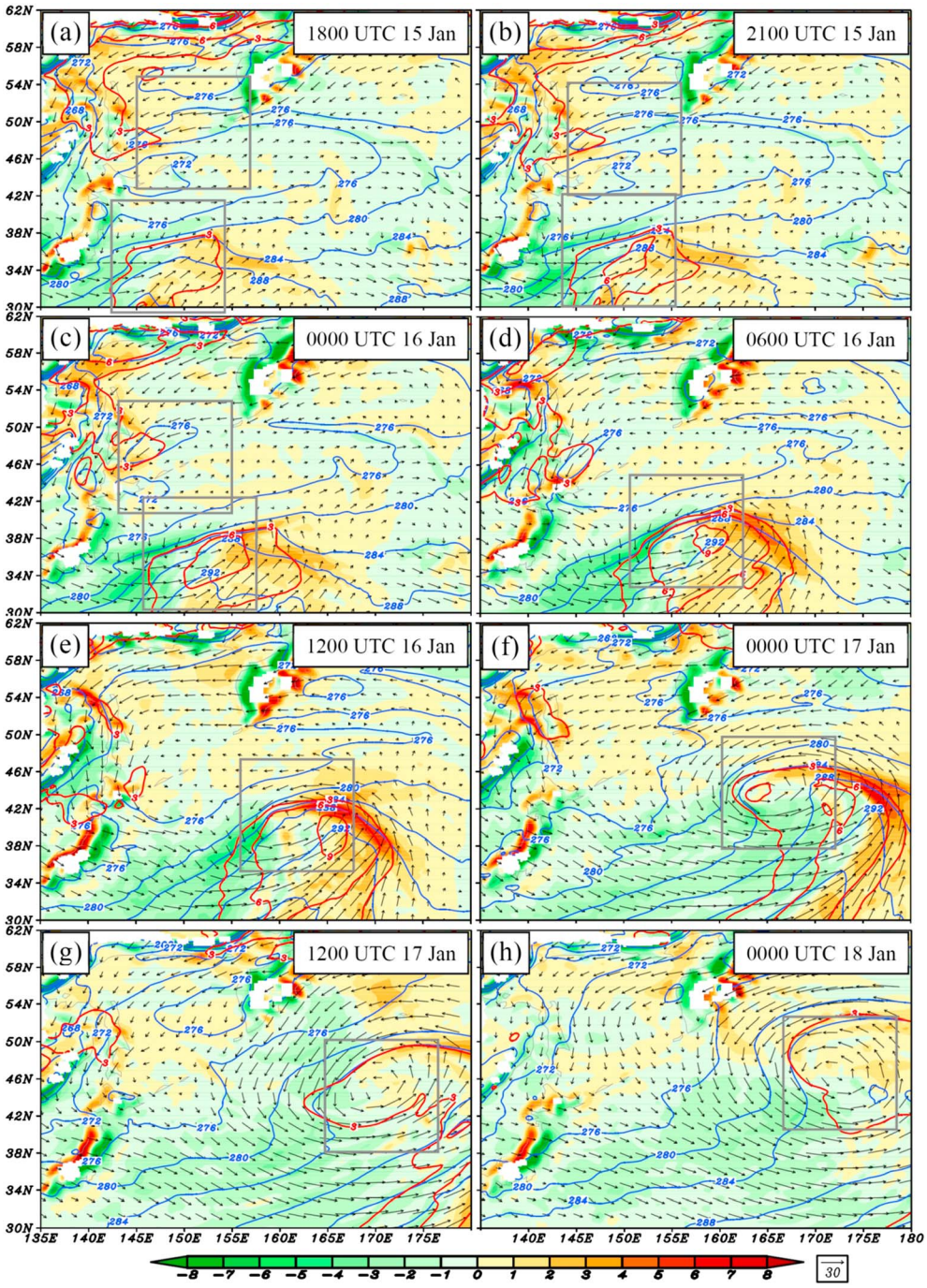

Figure 8. Potential temperature (blue solid line; units: K), potential temperature anomalies relative to the temporal mean of whole simulation period (red solid line; units: K), horizontal advection of temperature (shading; units: 10^{-4} K/s), and horizontal wind field (vector; units: m/s) at 900 hPa, where the boxes show key regions of the twin cyclones.

there. Over the Japanese archipelago, there was an upper level warm tongue (not shown), east of which warm advection appeared. The twin cyclones were both located beneath the warm tongue and warm advection (Figures 7a and 7b). However, because Cyclone A was under an upper level jet core (Figures 5a and 5b), its associated warm advection reached an intensity of up to 10^{-3} K/s, which was much stronger than that associated with Cyclone B (Figures 7a and 7b).

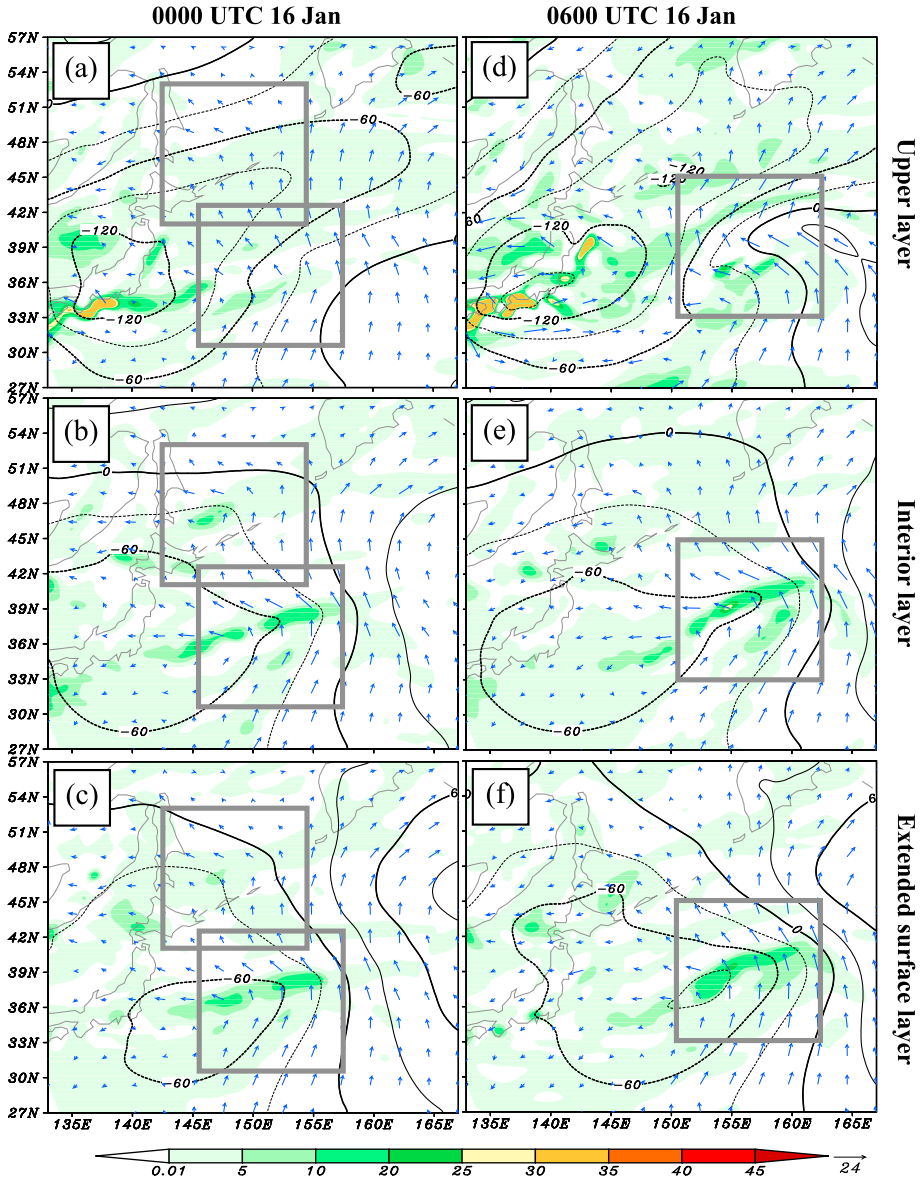

Figure 9. The 900-hPa geopotential height perturbation (black lines; units: gpm), wind perturbation (blue vector; units: m/s), and geostrophic vorticity perturbation (shading; units: 10^{-5}/s) associated with the PV anomalies (a, d) in the upper layer, (b, e) in the interior layer, and (c, f) in the extended surface layer. Grey boxes mark key regions of the twin cyclones.

In the middle troposphere, a low-pressure/height zone and a cold tongue stretched from the Japanese archipelago eastward (Figures 5a and 5b). Cyclone B was embedded within this low area and cold tongue, while Cyclone A was located ahead of a shortwave trough, south of the cold tongue. Calculation indicates that both the cyclonic-vorticity advection and warm advection were stronger for Cyclone A (not shown). As Figures 7a and 7b show, Cyclone A had more favorable moisture conditions and stronger ascending motions than Cyclone B. This resulted in heavier precipitation (not shown) and stronger positive PV anomalies in the middle and lower troposphere over Cyclone A (Figure 7b).

In the lower troposphere, similar to that in the middle troposphere, a cold tongue stretched from the Japanese archipelago eastward (Figures 8a and 8b). Cyclone B was located in the central and northern sections of the cold tongue. Warm/cold advection mainly appeared in the western/eastern section of Cyclone B. In contrast, Cyclone A was located south of the cold tongue (Figures 8a and 8b), with warm/cold

Table 3
Main Factors Accounting for the Significantly Different Deepening Rates of the Twin Cyclones During the Intense Interaction Stage (INT-IS) and Main Factors Dominating the Explosive Deepening of Cyclone A During the Maximum (MAX-DS) Stage

	Upper layer	Interior layer	Extended surface layer
INT-IS	None	Precipitation-Related Latent Heating	Temperature Advection
MAX-DS	Tropopause Folding	Precipitation-Related Latent Heating (Later Period)	Warm Advection (Earlier Period)

advection appearing in its southeastern/northwestern quadrants. Mainly due to the warm advection, positive θ anomalies formed/enhanced within the southeastern section of Cyclone A. Upward sensible heat flux (not shown) also contributed to the positive θ anomaly, but it was of secondary importance. According to Bretherton (1966), near-surface positive θ anomalies are equivalent to positive PV anomalies.

4. Mechanisms Governing Evolution of the Twin Cyclones

4.1. Intense Interaction Stage

4.1.1. PPVI Analysis of Cyclone Deepening

According to the PV budget equation (Koshyk & McFarlane, 1996), positive PV anomalies in the UL, ML, and ESL are mainly generated by tropopause folding, latent heating, and warm advection, respectively (Davis & Emanuel, 1991; Fu et al., 2014; Martin & Marsili, 2002). As Figures 9a–9c show, all these factors contributed to the twin cyclones' deepening in this stage. Based on the 900-hPa geopotential height perturbations, UL effects (tropopause folding) accounted for ~39% for the total height perturbations within key region A (Figure 9a), whereas the equivalent value for Cyclone B was more than 50%. The UL-associated negative height perturbations peaked over Honshu Island and stretched from the southwest to the northeast. This corresponded to the distribution of upper level positive PV anomalies that were generated primarily by tropopause folding (Figures 6a–6d). Maximum negative height perturbations appeared between the twin cyclones (Figure 9a). In contrast, the IL- and ESL-associated negative geopotential height perturbations were stronger in key region A. This was consistent with the comparisons of deepening rates (Figure 4c), precipitation (not shown), and lower level temperature advection (Figures 8a–8c) between the twin cyclones. Therefore, it can be concluded that although UL tropopause folding was the most important factor accounting for the deepening of the twin cyclones, the IL latent heating and the ESL warm advection were determining factors for the significant differences in their deepening rates (Table 3).

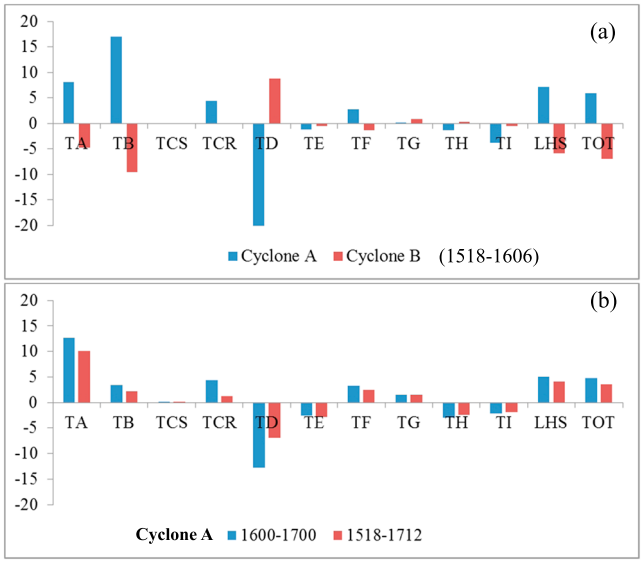

Figure 10. Panel (a) shows the temporal mean of key region-averaged Zwack-Okossi vorticity budget terms of Cyclones A and B (units: 10^{-10} s^{-2}), respectively, during the intense interaction stage (1518–1606). Panel (b) shows the temporal mean of key region-averaged Zwack-Okossi vorticity budget terms of Cyclone A (units: 10^{-10} s^{-2}) during the maximum development stage (1600–1700) and whole development period (1518–1712), respectively. LHS represents the left-hand side term (local time derivative), and TOT stands for the total effects of the right-hand side terms.

4.1.2. Zwack-Okossi Vorticity Budget of Cyclone Rotation

The 900-hPa geostrophic vorticity was remarkably different between Cyclones A and B. The Zwack-Okossi vorticity budget equation (Lupo et al., 1992) was used to show corresponding mechanisms. First, the terms of the equation were averaged within respective key regions. Then, a temporal mean (within different targeted stages) was calculated for each term to show its overall effect during this stage. For a term, vertical integrals within three layers of equal mass (900–650 hPa, 650–400 hPa, and 400–150 hPa) were compared to determine its most important layer. Results shown in Figure 10 indicate the local time derivative, which was calculated using a finite difference method with hourly outputs of MM5, and the sum of the right-hand side terms balance each other reasonably well (a relative error of below 19%). This guarantees the accuracy of the Zwack-Okossi vorticity budget analysis.

For Cyclone B, a negative local time derivative dominated its key region (Figure 10a), mainly due to the negative absolute-vorticity advection (term TA) and cold advection (term TB). In contrast, adiabatic warming

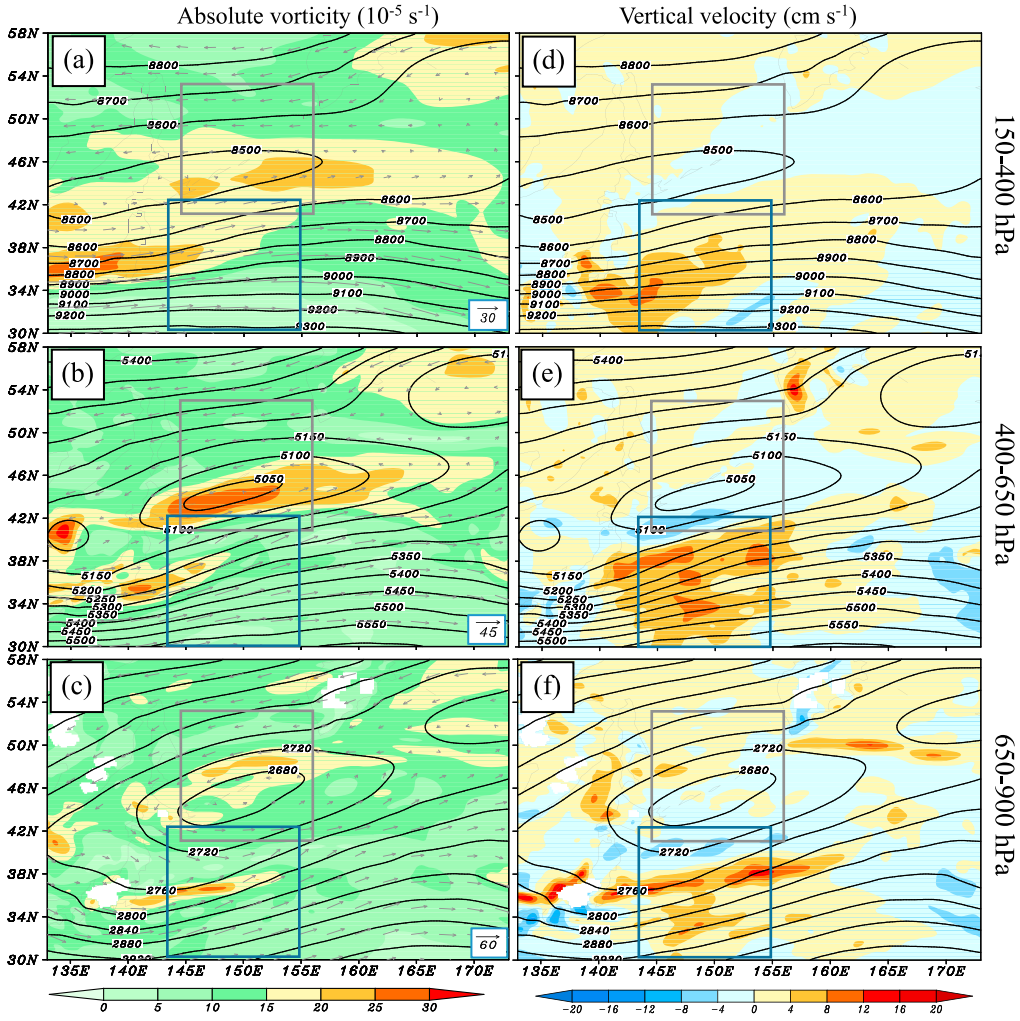

Figure 11. Panels (a–c) show the temporal mean (during the intense interaction stage) of the vertically averaged (refer to the layer shown on the right) absolute vorticity (shading; units: 10^{-5} s^{-1}), as well as the geopotential height (black solid line; units: gpm), and horizontal wind field (units: m/s) at typical levels (700 hPa, 500 hPa, and 300 hPa are used as typical levels for the lower troposphere, middle troposphere, and upper troposphere, respectively). Panels (d–f) show the temporal mean (during the intense interaction stage) of the vertically averaged (refer to the layer shown on the right) vertical velocity (shading; units: cm/s) and the geopotential height (black solid line; units: gpm) at typical levels. The boxes show key regions of the twin cyclones.

associated with descending motion (term TD) mainly offsets this decreasing trend. Within key region B, the maximum absolute vorticity appeared in the middle troposphere (Figures 11a–11c). Correspondingly, the strongest negative absolute-vorticity advection also appeared in this layer (Figures 12a–12c). Therefore, the middle-level negative advection of absolute vorticity was the main reason for the negative effect of term TA. Cold advection reached its maximum intensity in the lower troposphere of key region B (Figures 13a–13c) and decreased rapidly upward. This implies that lower level cold advection was the main factor accounting for the negative effect of term TB. Descending motions dominated key region B (Figures 11d–11f), with its maximum intensity appearing in the middle troposphere. Thus, the middle-level descending motions were the main reasons that term TD associated with Cyclone B was positive (Figure 10a).

For Cyclone A, a positive local time derivative appeared in its key region (Figure 10a). Warm advection (term TB) was the dominant factor for the increasing trend of geostrophic vorticity within key region A. From Figures 13a–13c, warm advection reached its maximum in the upper troposphere (because of the upper

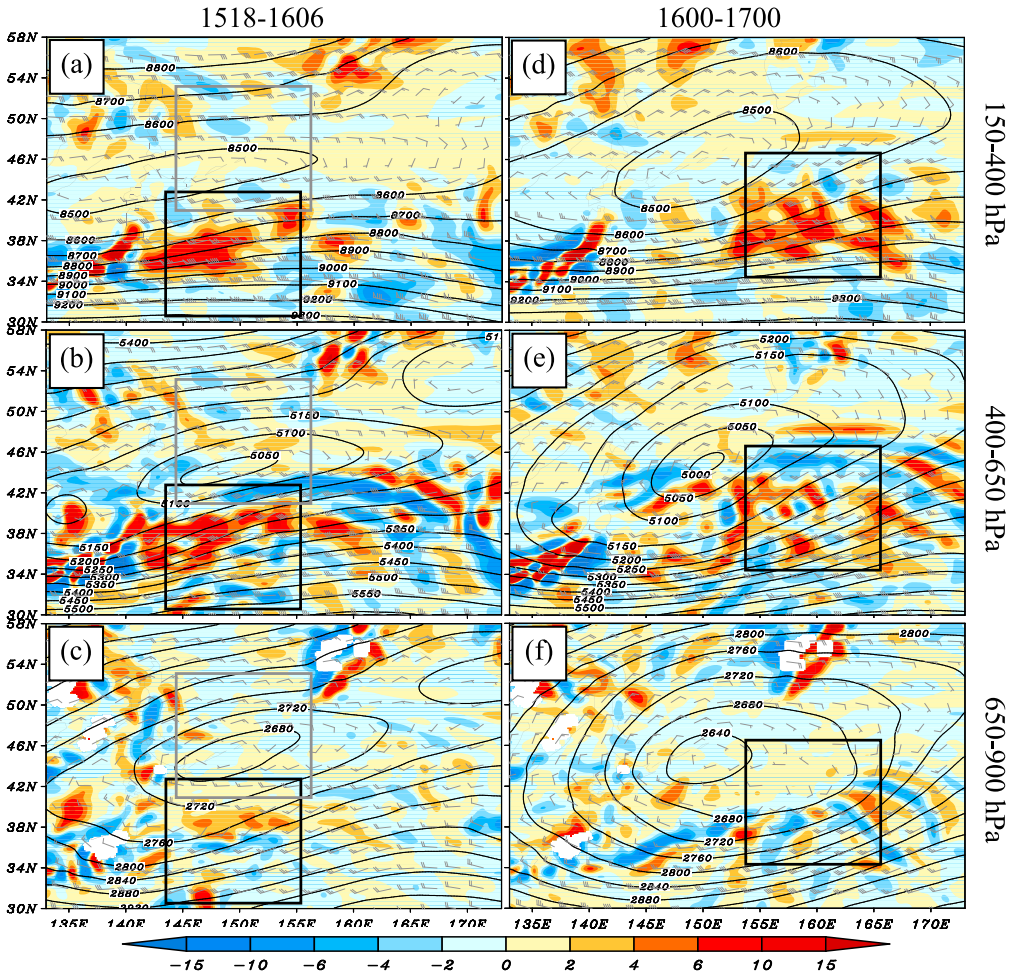

Figure 12. The temporal mean (refer to the period shown at top) of the vertically averaged (refer to the layer shown on the right) absolute-vorticity advection (shading; units: 10^{-9} s^{-2}), as well as the geopotential height (black solid lines; units: gpm), and horizontal wind field (a full bar represents 10 m/s) at typical levels (700 hPa, 500 hPa, and 300 hPa are used as typical levels for the lower troposphere, middle troposphere, and upper troposphere, respectively), where the boxes show key regions of the twin cyclones.

level jet). Thus, upper level warm advection was the dominant reason for the positive effect of term TB. The positive absolute-vorticity advection (term TA) and latent heating (term TCR) also contributed to the increase in geostrophic vorticity (Figure 10a). In contrast, adiabatic cooling due to ascending motion (term TD) offsets the increasing trend intensely. From Figures 12a–12c, the positive advection of absolute vorticity peaked in the upper troposphere because of the upper level jet and the strong cyclonic-vorticity center west of Cyclone A (Figure 11a). This upper level absolute-vorticity advection was the main factor for the positive effect of term TA. As Figures 11d–11f show, ascending motion dominated key region A and peaked in the middle troposphere. Therefore, the middle-level ascending motion was the most significant factor opposing the increasing trend of geostrophic vorticity.

Overall, TA (absolute-vorticity advection), TB (temperature advection), TCR (latent heating), and TD (vertical motion) governed the significantly different evolutionary trends of the twin cyclones (Figure 10a). For TA, the upper level positive advection within key region A and middle-level negative advection within key region B were what accounted most for the different behaviors of the twin cyclones (Figures 12a–12c). The upper level warm advection associated with Cyclone A and the lower level cold advection associated with Cyclone B were the main reasons for the significant differences of term TB in the twin cyclones (Figures 13a–13c). Cyclone A induced the heavier of the two precipitations because of its stronger

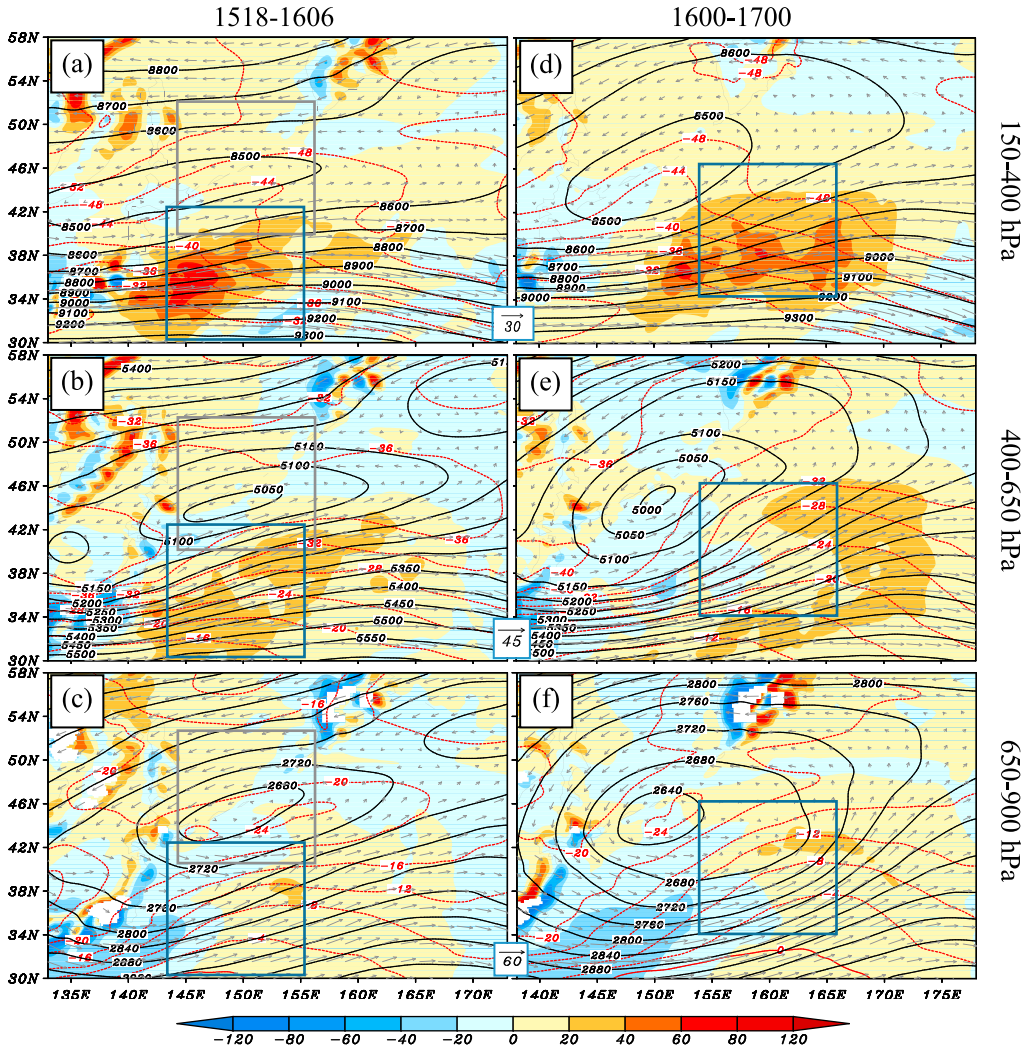

Figure 13. The temporal mean (refer to the period shown at top) of the vertically averaged (refer to the layer shown on the right) temperature advection (shading; units: 10^{-5} K/s), as well as the temperature (red dashed line; units: °C), geopotential height (black solid line; units: gpm), and horizontal wind field (units: m/s) at typical levels (700 hPa, 500 hPa, and 300 hPa are used as typical levels for the lower troposphere, middle troposphere, and upper troposphere, respectively), where the boxes show key regions of the twin cyclones.

ascending motion (Figures 11d–11f) and more abundant moisture (Figures 7a–7c). For adiabatic processes, the strongest vertical motions associated with the twin cyclones both appeared in the middle troposphere (Figures 11d– 11f), implying that the middle-level adiabatic warming/cooling processes were the primary reasons for the different effects of term TD on the twin cyclones (Table 4).

Table 4
Main Factors Accounting for the Significantly Different Evolutions of Geostrophic Vorticity Associated With the Twin Cyclones During the Intense Interaction Stage (INT-IS) and Main Factors Dominating the Increase of Geostrophic Vorticity Associated With Cyclone A During the Maximum (MAX-DS) Stage

	Upper troposphere (400–150 hPa)	Middle troposphere (650–400 hPa)	Lower troposphere (900–650 hPa)
INT-IS	Warm advection; positive absolute-vorticity advection	Negative absolute-vorticity advection; adiabatic warming/cooling associated with vertical motions	Cold advection; precipitation-related latent heating
MAX-DS	Positive absolute-vorticity advection	None	Precipitation-related latent heating

Note. For convenience, precipitation and its associated latent heating are given in the rightmost column.

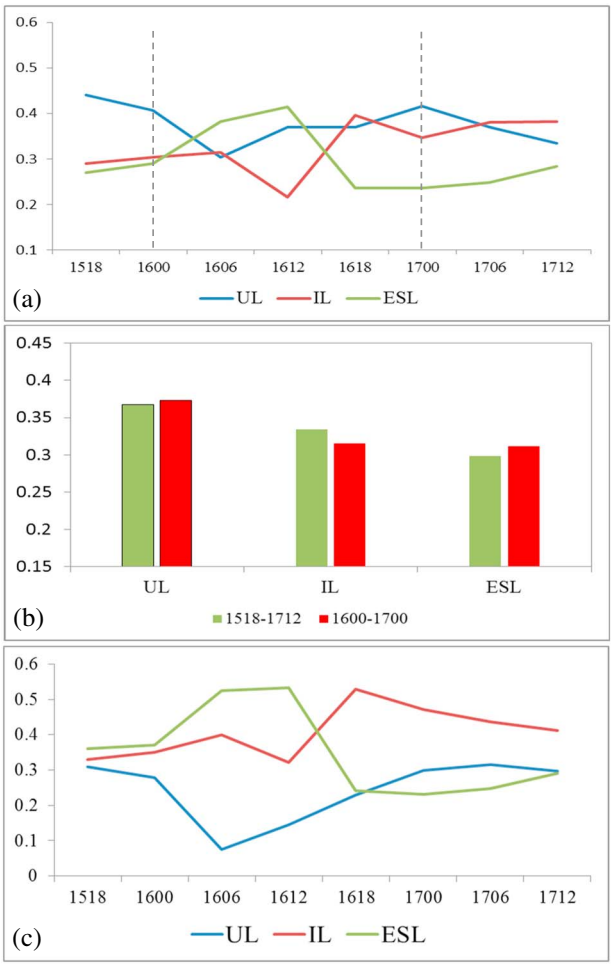

Figure 14. Panel (a) shows the relative contributions of the upper layer (UL), interior layer (IL), and extended surface layer (ESL) to the total geopotential perturbation at 900 hPa, based on the key region average of Cyclone A. Panel (b) shows the temporal mean of the time series in panel (a) during the whole development period and the maximum development stage (between the dashed lines), respectively. Panel (c) is the same as panel (a), but for the horizontal average in A2 (Figure 4a).

4.2. Maximum Development Stage of Cyclone A

4.2.1. PPVI Analysis of Cyclone Deepening

Cyclone A intensified rapidly after formation, with its maximum deepening rate of 2.6 Bergeron appearing in the maximum development stage (Table 2). According to PPVI analysis (Figure 14a), the relative contributions of the effects from the UL, IL, and ESL varied significantly with time. Before 0000 UTC 16 January, the tropopause-folding-related PV anomalies (Figures 6a–6c) accounted for the largest negative geopotential height perturbations (Figure 14a), while the PV anomalies due to latent heating in the IL (Figures 7a and 7b) and warm advection in the ESL (Figures 8a–8c) were of approximately the same importance (Figure 14a). From 0000 UTC to 1200 UTC 16 January, the lower level wind associated with Cyclone A intensified rapidly (Figures 5b–5c), which enhanced the northward warm advection (Figures 8c–8e). This induced a significant increase in positive θ anomalies associated with Cyclone A. In addition, strong upward sensible heat flux also favored intensification of these positive anomalies (not shown). Therefore, ESL effects became the most important factor in sustaining the rapid deepening of Cyclone A during this period (Figure 14a). From 1200 UTC 16 to 1200 UTC 17 January, although the lower level wind remained strong (Figures 5c–5e), the cold and warm fronts associated with Cyclone A weakened significantly, which was reflected in the rapidly reducing density of isolines of θ (Figures 8e–8g). Correspondingly, within the key region A, warm advection weakened and cold advection enlarged in the area, both of which reduced the positive θ anomalies. Therefore, the effects of the ESL decreased (Figure 14a), becoming the least important contribution. In contrast, positive PV anomalies associated with latent heating in the IL grew rapidly from 1200 UTC to 1800 UTC 16 January (Figures 7d–7e) because of the significant enhancement in precipitation (not shown) and then maintained their strong intensity (Figures 7e–7h). Correspondingly, the contribution of the IL also grew rapidly and became one of the two dominant factors sustaining the deepening of Cyclone A (Figure 14a). The other dominant factor was positive PV anomalies in the UL, which maintained their strength because the tropopause-folding processes remained strong over Cyclone A (Figures 7d–7h).

Overall, during the maximum development stage, the tropopause folding in the UL contributed the most (~37%) to the rapid development of Cyclone A (Figure 14b), while the latent heating in the IL ranked second, contributing slightly more than the ESL warm advection. Although UL effects contributed the most to the lowering of geopotential height within key region A, strong centers of negative height perturbation were closely related to effects in the IL (Figures 15e and 16b) and ESL (Figure 16f). These strong centers generally covered the locations of the minimum SLP of Cyclone A, where the extreme deepening rate occurred. Therefore, IL and ESL effects might be crucial for the extreme deepening at/around locations of minimum SLP. As shown in Figure 4a, the extreme deepening rate (Point and A2) has a much larger slope than that of the A12-averaged deepening rate. Because the A2-averaged trend was the most similar to that at the location of the minimum SLP, A2 was used to evaluate the relative contributions of different factors to the extreme deepening rate. A further comparison indicates that the Point, A2, and A4 in Figure 4a showed a similar relative importance of each factor in the extreme deepening rate. The overall state of deepening can be represented by the averages over A6–A20, each of which showed a similar relative importance to that illustrated in Figure 14b. Comparisons between Figures 14a and 14c show that averages in regions of different size did not modify the main variational trend of an individual factor's contribution. However, the relative importance of each factor changed significantly. For the extreme deepening rate, UL effects contributed the least (~21%). Strong ESL warm advection dominated the period from 0000 UTC to

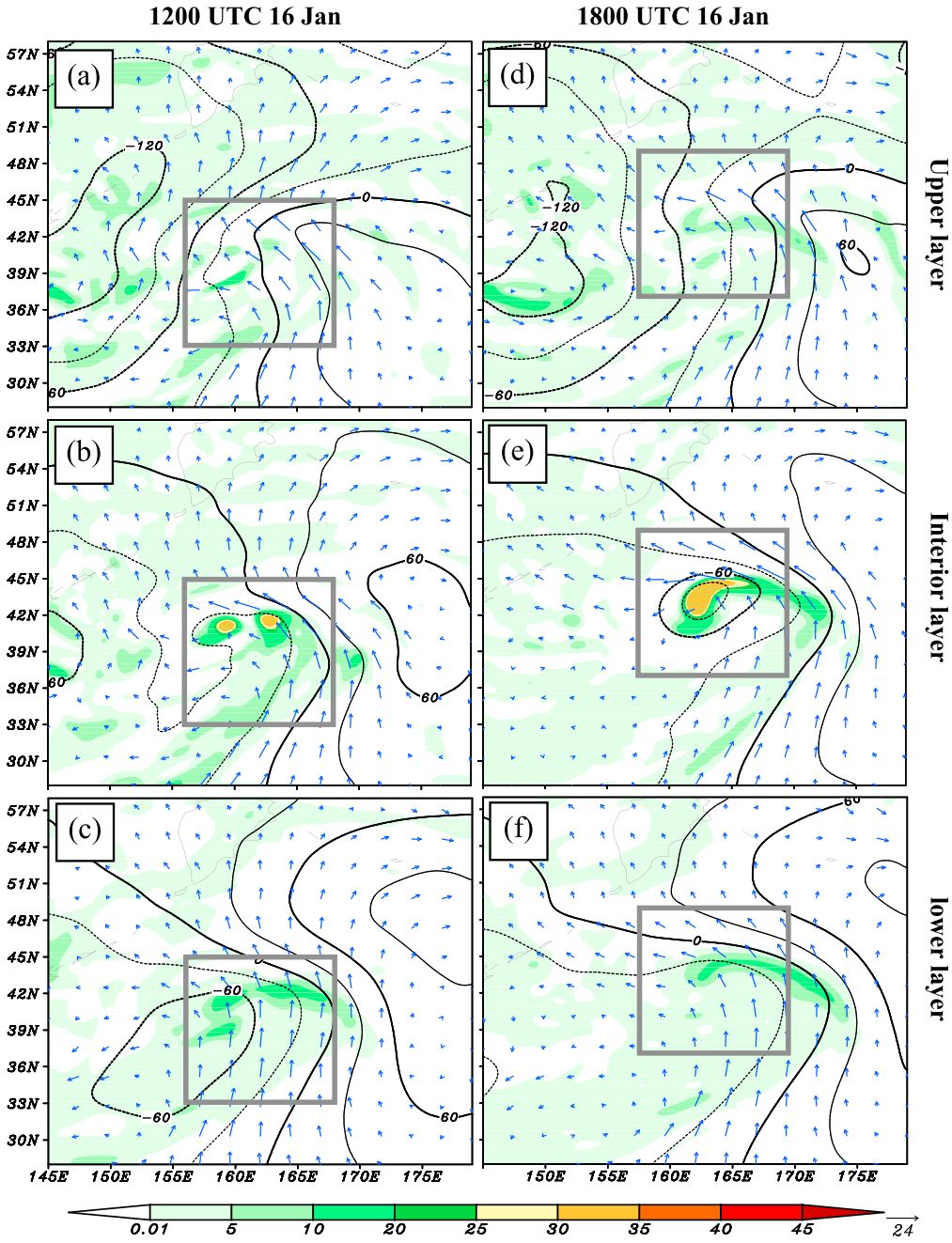

Figure 15. The same as Figure 9 but forr 12 h later.

1200 UTC 16 January (~49%) (Figure 14c), and strong latent heating in the IL governed the period from 1800 UTC 16 to 1200 UTC 17 January (~47%). This implies that warm advection and latent heating were necessary for the extreme deepening. Moreover, a fake dry run showed that a removal of latent heating shortened the explosive development time significantly (Figure 2b), and the maximum deepening rate was also reduced sharply (Table 2).

4.2.2. Zwack-Okossi Vorticity Budget of Cyclone Rotation

After formation, the geostrophic vorticity of Cyclone A grew rapidly (Figure 4d), mainly due to term TA (Figure 10b). As Figures 12d–12f show, the positive absolute-vorticity advection peaked in the upper troposphere (because of the upper level jet) and decreased downward. This means that the upper level

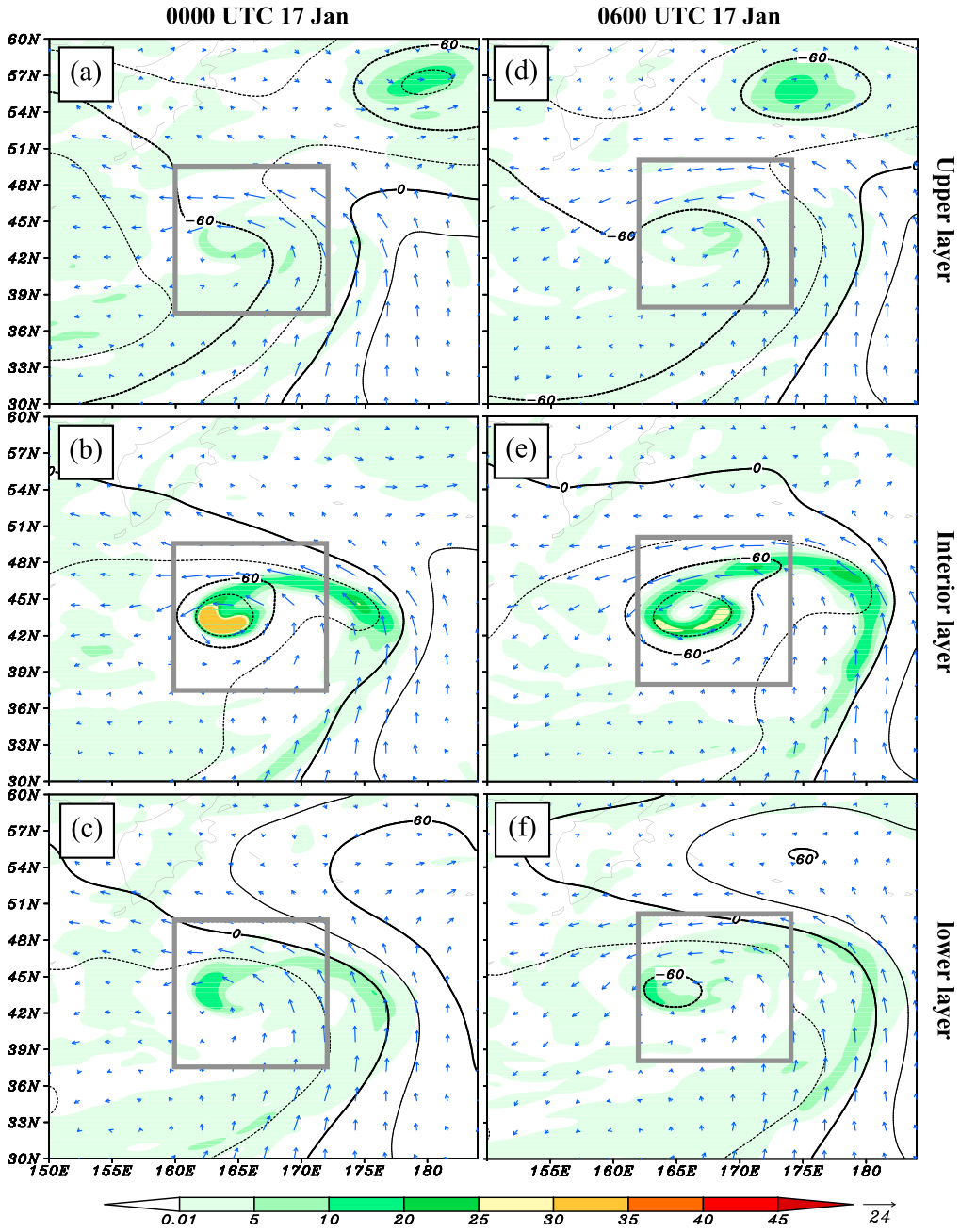

Figure 16. The same as Figure 9 but for 24 hr later.

positive advection of absolute vorticity was crucial to the increase in geostrophic vorticity associated with Cyclone A. Term TCR (latent heating) is the second most important factor contributing to the increase in geostrophic vorticity (Figure 10b). Term TB also favored the increase in geostrophic vorticity, but it decreased significantly in intensity compared with that during the intense interaction stage (cf. Figures 10a and 10b). The intensification of cold advection and weakening of warm advection in the middle troposphere of key region A (cf. Figures 13b and 13e) was the main reason for TB's reducing effect. Intense ascending motion dominated key region A, which resulted in a negative TD term because of adiabatic cooling (Figure 10b). This was the most significant factor resisting the increase in geostrophic vorticity associated with Cyclone A.

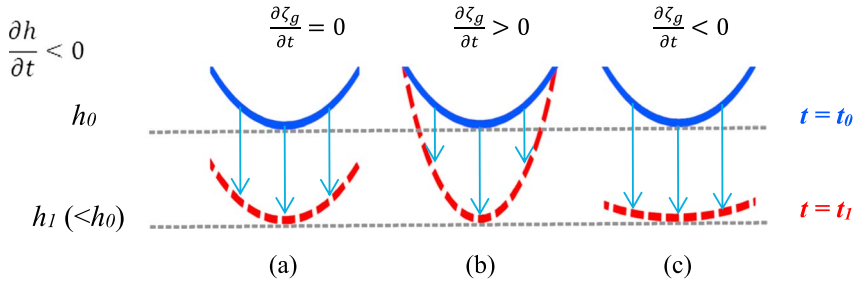

Figure 17. Schematic cross sections of the deepening of (geopotential) height associated with a cyclone, where the blue solid line shows the original state of an isohypsic surface(at $t = t_0$), the red dashed line shows the final state of this isohypsic surface (at $t = t_1$),thin arrows represent the height decreased, h represents the geopotential height, and ζ_g denotes the geostrophic vorticity.

5. Conclusion and Discussion

This study investigated mechanisms accounting for the evolutions of twin extratropical cyclones, one of which was an EEC, over the northwest Pacific Ocean during mid-January 2011. The cyclonic relative rotation of the twin cyclones was confirmed to be a Fujiwhara effect. In addition to influencing each other's movement, the interaction of the twin extratropical cyclones also influenced their intensity and structure. An additional PPVI analysis was applied to the PV anomalies in the ESL that were associated with the twin cyclones (i.e., only the positive PV anomalies within key region A/B were kept, and PPVI was conducted, which can show the effects of Cyclone A/B on Cyclone B/A) to show interactions between them. Results indicated that, overall, the wind perturbations associated with Cyclone A induced warm advection within the key region of Cyclone B, whereas the wind perturbations associated with Cyclone B induced cold advection within the key region of Cyclone A (not shown). This meant that Cyclone B weakened Cyclone A through inducing cold advection (decelerating the intensification of rotation and the lowering of pressure), whereas Cyclone A enhanced Cyclone B through inducing warm advection.

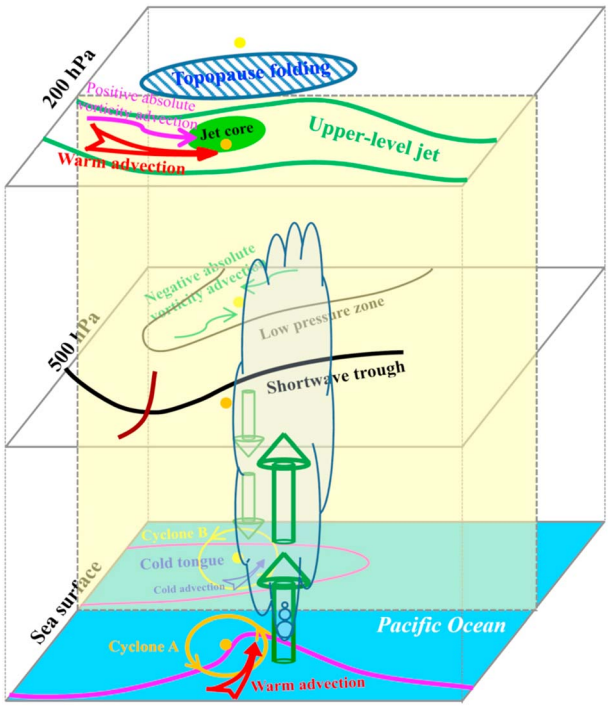

Figure 18. Schematic illustration of the mechanisms accounting for the significantly different evolutions of the twin cyclones, where the purple solid lines at the sea surface represent the isotherm, the orange circle with orange dots stands for the Cyclone A, the yellow cyclone with yellow dots represents the Cyclone B, the black solid line at 500-hPa surface is the isohypse, green solid line at 200 hPa is the isotach, the green shading ellipse represents the jet core above 100 m/s, and the dark blue ellipse stands for the regions having strong tropopause folding. The green open arrow stands for vertical motions (the dark blue curved line shows the cloud), and the red and blue open arrows are the warm and cold advection, respectively. The purple and green solid curved arrows are the positive and negative absolute-vorticity advection, respectively. The big yellow shading box is used to separate the conditions of Cyclones A and B.

In this event, Cyclone B was initially stronger than Cyclone A, but the latter was under more favorable conditions, which contributed to its faster development. It took ~6 hr for Cyclone A to reach a similar intensity to that of Cyclone B. Then, the intensity contrast reversed. Under this situation, Cyclone B began to merge into Cyclone A. The merging was completed at 1800 UTC 16 January, which obviously did not accelerate the development of Cyclone A (Figure 4d).

The evolution of rotation and deepening of a cyclone may not be consistent with each other. For Cyclone B, it was similar to the situation shown in Figure 17a, in which the isohypsic surface lowered while its curvature changed little. For cyclone A, it was similar to that shown in Figure 17b, in which both deepening and rotation enhanced simultaneously. Because geostrophic vorticity represents the curvature of an isohypsic surface, the isohypsic surface curvature increased as the isohypsic surface lowered. Thus, it may be necessary to investigate a cyclone's deepening and rotation separately. In this study, PPVI analysis showed a strong UL positive PV anomaly due to tropopause folding persisting between the twin cyclones and served as the most favorable factor for their deepening. However, this was not a key reason for the significant differences in the deepening rates of Cyclones A and B.

Rather, the IL latent heating and the ESL warm advection, which were much stronger for Cyclone A, were the determining factors for its much larger deepening rate (Table 3). The Zwack-Okossi vorticity budget showed that the contrast between the upper tropospheric positive absolute-vorticity advection (Cyclone A) and the middle tropospheric negative absolute-vorticity advection (Cyclone B), the contrast between the upper tropospheric warm advection (Cyclone A) and the lower tropospheric cold advection (Cyclone B), as well as the contrast between precipitation and middle tropospheric vertical motion associated with Cyclones A and B, accounted for the significantly different variations of geostrophic vorticity of the twin cyclones (Table 4). In summary, a schematic illustration of the mechanisms accounting for the significantly different evolutions of the twin cyclones is given in Figure 18.

Cyclone A developed into an extreme EEC whose intensity was comparable with that of a typhoon. The PPVI analysis showed that tropopause folding in the UL and warm advection in the ESL dominated the earlier stage of its explosive deepening (Figure 14a). Then, during the later stage, the latent heating-produced positive PV anomalies intensified significantly in the IL as precipitation increased. This induced a remarkable enhancement in their associated negative geopotential height perturbations. Therefore, the latent heating in the IL and tropopause folding in the UL were the main factors in sustaining the explosive deepening of Cyclone A during this stage. Overall, the factors accounting for the explosive deepening of the EEC showed significant scale dependence: forcing in the UL contributed more as the horizontal scale increased, whereas forcing in the IL and ESL contributed a larger proportion as the horizontal scale decreased.

The Zwack-Okossi vorticity budget showed that the upper tropospheric positive absolute-vorticity advection associated with the upper level jet and the latent heating were crucial to the increase in geostrophic vorticity associated with Cyclone A, whereas adiabatic cooling due to ascending motion was the most important factor opposing the increase in geostrophic vorticity. Comparison of the relative configuration of Cyclone A and the upper level jet showed that during the maximum development stage, explosive deepening of Cyclone A showed no sensitive responses to this configuration (Figure 2b), whereas the rotation enhancement of Cyclone A was faster when it was embedded within the upper level jet (Figure 4d).

Unlike the extreme EECs over the northwestern Pacific Ocean reported by Kuwano-Yoshida and Asuma (2008) and Fu et al. (2014), which showed significant responses to latent heating-related nonlinear processes (removal of latent heating caused the extreme EEC to become a nonexplosive cyclone), the extreme EEC in this study showed much less sensitivity to latent heating (removing latent heating rendered a reduction of only ~38% of the EEC deepening rate). The fake dry sensitivity run showed that an EEC can form without any support from latent heating (Table 2).

Acknowledgments
The authors are grateful to the NCEP, NASA, NOAA, and JMA for providing the data (http://rda.ucar.edu/datasets; https://gcmd.nasa.gov/records/GC%20MD_REYNOLDS_SST.html; https://pmm.nasa.gov/data-access/downloads/trmm; http://www.jma.go.jp/jma/menu/menureport.html). This research was supported by the National Key R&D Program of China (2017YFC1501804), the National Natural Science Foundation of China (41775046 and 91637211), and the Youth Innovation Promotion Association, Chinese Academy of Sciences.

References

Allen, J. T., Pezza, A. B., & Black, M. T. (2010). Explosive cyclogenesis: A global climatology comparing multiple reanalyses. *Journal of Climate*, *23*(24), 6468–6484. https://doi.org/10.1175/2010JCLI3437.1

Azad, R., & Sorteberg, A. (2014). The vorticity budgets of North Atlantic winter extratropical cyclone life cycles in MERRA reanalysis. Part I: Development phase. *Journal of the Atmospheric Sciences*, *71*(9), 3109–3128. https://doi.org/10.1175/JAS-D-13-0267.1

Black, M. T., & Pezza, A. B. (2013). A universal, broad environment energy conversion signature of explosive cyclones. *Geophysical Research Letters*, *40*, 452–457. https://doi.org/10.1002/grl.50114

Brand, S. (1970). Interaction of binary tropical cyclones of the western North Pacific Ocean. *Journal of Applied Meteorology*, *9*(3), 433–441. https://doi.org/10.1175/1520-0450(1970)009%3C0433:IOBTCO%3E2.0.CO;2

Bretherton, F. P. (1966). Critical layer instability in baroclinic flows. *Quarterly Journal of the Royal Meteorological Society*, *92*(393), 325–334. https://doi.org/10.1002/qj.49709239302

Charney, J. G. (1955). The use of primitive equations of motion in numerical prediction. *Tellus*, *7*, 22–26.

Chen, T.-C., Tsay, J.-D., Yen, M.-C., & Cayanan, E. O. (2010). Formation of the Philippine twin tropical cyclones during the 2008 summer monsoon onset. *Monthly Weather Review*, *25*, 1317–1341.

Davis, C. A., & Emanuel, K. A. (1991). Potential vorticity diagnostics of cyclogenesis. *Monthly Weather Review*, *119*(8), 1929–1953. https://doi.org/10.1175/1520-0493(1991)119%3C1929:PVDOC%3E2.0.CO;2

Davis, C. A., Grell, E. D., & Shapiro, M. A. (1996). The balanced dynamical nature of a rapidly intensifying oceanic cyclone. *Monthly Weather Review*, *124*(1), 3–26. https://doi.org/10.1175/1520-0493(1996)124%3C0003:TBDNOA%3E2.0.CO;2

Davis, C. A., Stoelinga, M. T., & Kuo, Y. H. (1993). The integrated effect of condensation in numerical simulations of extratropical cyclogenesis. *Monthly Weather Review*, *121*(8), 2309–2330. https://doi.org/10.1175/1520-0493(1993)121%3C2309:TIEOCI%3E2.0.CO;2

Dong, K.-Q., & Neumann, C. J. (1983). On the relative motion of binary tropical cyclones. *Monthly Weather Review*, *111*(5), 945–953. https://doi.org/10.1175/1520-0493(1983)111%3C0945:OTRMOB%3E2.0.CO;2

Dudhia, J. (1989). Numerical study of convection observed during the Winter Monsoon Experiment using a mesoscale two-dimensional model. *Journal of the Atmospheric Sciences*, *46*(20), 3077–3107. https://doi.org/10.1175/1520-0469(1989)046%3C3077:NSOCOD%3E2.0.CO;2

Ertel, H. (1942). Ein neuer hydrodynamischer wirbelsatz. *Meteorologische Zeitschrift*, *59*, 271–281.

Fu, S.-M., Sun, J.-H., & Sun, J.-R. (2014). Accelerating two-stage explosive development of an extratropical cyclone over the northwestern Pacific Ocean: A piecewise potential vorticity diagnosis. *Tellus*, *66*(1), 23210. https://doi.org/10.3402/tellusa.v66.23210

Fujiwhara, S. (1923). On the growth and decay of vortical systems. *Quarterly Journal of the Royal Meteorological Society*, *49*, 75–104.

Grell, G. A. (1993). Prognostic evaluation of assumptions used by cumulus parameterizations. *Monthly Weather Review*, *121*(3), 764–787. https://doi.org/10.1175/1520-0493(1993)121%3C0764:PEOAUB%3E2.0.CO;2

Grell, G. A., Dudhia, J., & Stauffer, D. R. (1995). A description of the Fifth-Generation Penn State/NCAR Mesoscale Model (MM5). NCAR tech. Note NCAR/TN_398_STR (122 pp.).

Hakim, G. J., Keyser, D., & Bosart, L. F. (1996). The Ohio Valley wave-merger cyclogenesis event of 25–26 January 1978. Part II: Diagnosis using quasigeostrophic potential vorticity inversion. *Monthly Weather Review*, *124*(10), 2176–2205. https://doi.org/10.1175/1520-0493(1996)124%3C2176:TOVWMC%3E2.0.CO;2

Haurwitz, B. (1951). The motion of binary tropical cyclones. *Archiv für Meteorologie, Geophysik und Bioklimatologie, Serie A*, *4*, 73–86.

Hirata, H., Kawamura, R., Kato, M., & Shinoda, T. (2015). Influential role of moisture supply from the Kuroshio/Kuroshio extension in the rapid development of an extratropical cyclone. *Monthly Weather Review*, *143*(10), 4126–4144. https://doi.org/10.1175/MWR-D-15-0016.1

Hoover, E. W. (1961). Relative motion of hurricane pairs. *Monthly Weather Review*, *89*(7), 251–255. https://doi.org/10.1175/1520-0493(1961)089%3C0251:RMOHP%3E2.0.CO;2

Huffman, G. J. (1997). Estimates of root-mean-square random error contained in finite sets of estimated precipitation. *Journal of Applied Meteorology*, *36*(9), 1191–1201. https://doi.org/10.1175/1520-0450(1997)036%3C1191:EORMSR%3E2.0.CO;2

Jang, W., & Chun, H. Y. (2013). The effects of topography on the evolution of Typhoon ST Saomai (2006) under the influence of TS Bopha (2006). *Monthly Weather Review*, *141*(2), 468–489. https://doi.org/10.1175/MWR-D-11-00241.1

Keen, R. A. (1982). The role of cross-equatorial tropical cyclone pairs in the southern oscillation. *Monthly Weather Review*, *110*(10), 1405–1416. https://doi.org/10.1175/1520-0493(1982)110%3C1405:TROCET%3E2.0.CO;2

Koshyk, J. N., & McFarlane, N. A. (1996). The potential vorticity budget of an atmospheric general circulation model. *Journal of the Atmospheric Sciences*, *53*(4), 550–563. https://doi.org/10.1175/1520-0469(1996)053%3C0550:TPVBOA%3E2.0.CO;2

Kuwano-Yoshida, A., & Asuma, Y. (2008). Numerical study of explosively developing extratropical cyclones in the northwestern Pacific region. *Monthly Weather Review*, *136*(2), 712–740. https://doi.org/10.1175/2007MWR2111.1

Liu, H.-Y., & Tan, Z.-M. (2016). A dynamical initialization scheme for binary tropical cyclones. *Monthly Weather Review*, *144*(12), 4787–4803. https://doi.org/10.1175/MWR-D-16-0176.1

Lupo, A. R., Smith, P. J., & Zwack, P. (1992). A diagnosis of the explosive development of two extratropical cyclones. *Monthly Weather Review*, *120*(8), 1490–1523. https://doi.org/10.1175/1520-0493(1992)120%3C1490:ADOTED%3E2.0.CO;2

Martin, J. E., & Marsili, N. (2002). Surface cyclolysis in the North pacific Ocean. Part II: Piecewise potential vorticity diagnosis of a rapid cyclolysis event. *Monthly Weather Review*, *130*, 1264–1281.

Martin, J. E., & Otkin, J. A. (2004). The rapid growth and decay of an extratropical cyclone over the central Pacific Ocean. *Weather Forecasting*, *19*(2), 358–376. https://doi.org/10.1175/1520-0434(2004)019%3C0358:TRGADO%3E2.0.CO;2

Parsons, K. E., & Smith, P. J. (2004). An investigation of extratropical cyclone development using a scale-separation technique. *Monthly Weather Review*, *132*(4), 956–974. https://doi.org/10.1175/1520-0493(2004)132%3C0956:AIOECD%3E2.0.CO;2

Prieto, R., McNoldy, B. D., Fulton, S. R., & Schubert, W. H. (2003). A classification of binary tropical cyclone-like vortex interactions. *Monthly Weather Review*, *131*(11), 2656–2666. https://doi.org/10.1175/1520-0493(2003)131%3C2656:ACOBTC%3E2.0.CO;2

Qi, G.-Y. (1993). Climatic characteristics of explosive cyclone over the North Pacific Ocean. *Quarterly Journal of Applied Meteorology*, *4*, 426–433.

Reisner, J. R., Rasmussen, J., & Bruintjes, R. T. (1998). Explicit forecasting of supercooled liquid water in winter storm using the MM5 mesoscale model. *Quarterly Journal of the Royal Meteorological Society*, *124B*, 1071–1107.

Reynolds, R. W., Rayner, N. A., Smith, T. M., & Stokes, D. C. (2002). An improved in situ and satellite SST analysis for climate. *Journal of Climate*, *15*(13), 1609–1625. https://doi.org/10.1175/1520-0442(2002)015%3C1609:AIISAS%3E2.0.CO;2

Roebber, P. J., & Schumann, M. R. (2011). Physical processes governing the rapid deepening tail of maritime cyclogenesis. *Monthly Weather Review*, *139*(9), 2776–2789. https://doi.org/10.1175/MWR-D-10-05002.1

Sanders, F., & Gyakum, J. R. (1980). Synoptic-dynamic climatology of the "bomb". *Monthly Weather Review*, *128*, 2920–2934.

Schreck, C. J., & Molinari, J. (2009). A case study of an outbreak of twin tropical cyclones. *Monthly Weather Review*, *137*(3), 863–875. https://doi.org/10.1175/2008MWR2541.1

Sinclair, M. R. (1997). Objective identification of cyclones and their circulation intensity, and climatology. *Weather Forecasting*, *12*(3), 595–612. https://doi.org/10.1175/1520-0434(1997)012%3C0595:OIOCAT%3E2.0.CO;2

Spengler, T., & Egger, J. (2012). Potential vorticity attribution and causality. *Journal of the Atmospheric Sciences*, *69*(8), 2600–2607. https://doi.org/10.1175/JAS-D-11-0313.1

Wu, L. T., Martin, J. E., & Petty, G. W. (2011). Piecewise potential vorticity diagnosis of the development of a polar low over the Sea of Japan. *Tellus*, *63*, 198–211.

Yamamoto, M. (2012). Rapid merger and recyclogenesis of twin extratropical cyclones leading to heavy precipitation around Japan on 9–10 October 2001. *Meteorological Applications*, *19*(1), 36–53. https://doi.org/10.1002/met.255

Ying, M., Zhang, W., Yu, H., Lu, X., Feng, J., Fan, Y., et al. (2014). An overview of the China Meteorological Administration tropical cyclone database. *Journal of Atmospheric and Oceanic Technology*, *31*(2), 287–301. https://doi.org/10.1175/JTECH-D-12-00119.1

Yoshida, A., & Asuma, Y. (2004). Structures and environment of explosively developing extratropical cyclones in the northwestern Pacific region. *Monthly Weather Review*, *132*(5), 1121–1142. https://doi.org/10.1175/1520-0493(2004)132%3C1121:SAEOED%3E2.0.CO;2

Ziv, B., & Alpert, P. (1995). Rotation of binary cyclones—A data analysis study. *Journal of the Atmospheric Sciences*, *52*(9), 1357–1369. https://doi.org/10.1175/1520-0469(1995)052%3C1357:ROBCDA%3E2.0.CO;2

Ziv, B., & Alpert, P. (2003). Rotation of mid-latitude binary cyclones: A potential vorticity approach. *Theoretical and Applied Climatology*, *76*(3-4), 189–202. https://doi.org/10.1007/s00704-003-0011-x